Characteristics of Interannual Variability in Space-based XCO$_2$ Global Observations

Yifan Guan[1], Gretchen Keppel-Aleks[1], Scott C. Doney[2], Christof Petri[3], Dave Pollard[4], Debra Wunch[5], Frank Hase[6], Hirofumi Ohyama[7], Isamu Morino[7], Justus Notholt[3], Kei Shiomi[9], Kim Strong[5], Rigel Kivi[10], Matthias Buschmann[3], Nicholas Deutscher[12], Paul Wennberg[11], Ralf Sussmann[8], Voltaire A. Velazco[12,13], Yao Té[14]

[1]Department of Climate and Space Sciences and Engineering, University of Michigan, Ann Arbor, MI, 48105, USA
[2]Department of Environmental Sciences, University of Virginia, Charlottesville, VA, 22903, USA
[3]Institute of Environmental Physics, Physics Department, University of Bremen, Bremen, 28359, Germany
[4]National Institute of Water and Atmospheric Research, Omakau, 9377, New Zealand
[5]Department of Physics, University of Toronto, Toronto, M5S 1A7, Canada
[6]Institute of Meteorology and Climate Research - Atmospheric Trace Gases and Remote Sensing, Karlsruhe Institute of Technology, Eggenstein-Leopoldshafen, 76344, Germany
[7]National Institute for Environmental Studies, Tsukuba, Ibaraki 305-0053, Japan
[8]Institute of Meteorology and Climate Research - Atmospheric Environmental Research, Karlsruhe Institute of Technology, Garmisch-Partenkirchen, 82467, Germany
[9]Earth Observation Research Center, Japan Aerospace Exploration Agency, Tsukuba, Ibaraki, 305-8505, Japan
[10]Space and Earth Observation Centre, Finnish Meteorological Institute, Sodankylä, 99600, Finland
[11]Divisions of Engineering and Applied Science and Geological and Planetary Science, California Institute of Technology, Pasadena, CA, 91125, USA
[12]Centre for Atmospheric Chemistry, School of Earth, Atmospheric and Life Sciences, University of Wollongong, Wollongong, 2522, Australia
[13]Deutscher Wetterdienst, Meteorological Observatory, Hohenpeissenberg, 82383, Germany
[14]Laboratoire d'Etudes du Rayonnement et de la Matière en Astrophysique et Atmosphères, French National Centre for Scientific Research, Paris, 75016, France

Correspondence to: Yifan Guan (guanyf@umich.edu)

Abstract. Atmospheric carbon dioxide (CO$_2$) accounts for the largest radiative forcing among anthropogenic greenhouse gases. There is, therefore, a pressing need to understand the rate at which CO$_2$ accumulates in the atmosphere, including the interannual variations (IAV) in this rate. IAV in the CO$_2$ growth rate is a small signal relative to the long-term trend and the mean annual cycle of atmospheric CO$_2$, and IAV is tied to climatic variations that may provide insights into long-term carbon-climate feedbacks. Observations from the Orbiting Carbon Observatory-2 (OCO-2) mission offer a new opportunity to refine our understanding of atmospheric CO$_2$ IAV since the satellite can measure over remote terrestrial regions and the open ocean where traditional in situ CO$_2$ monitoring is difficult, providing better spatial coverage compared to ground-based monitoring techniques. In this study, we analyze the IAV of column-averaged dry air CO$_2$ mole fraction (XCO$_2$) from OCO-2 between September 2014 to June 2021. The amplitude of IAV variations, which is calculated as the standard deviation of the timeseries, is up to 1.2 ppm over the continents and around 0.4 ppm over the open ocean. Across all latitudes, the OCO-2 detected XCO$_2$ IAV shows a clear relationship with ENSO-driven variations that originate in the tropics and are transported poleward. Similar, but smoother, zonal patterns of OCO-2 XCO$_2$ IAV timeseries compared to ground-based in situ observations and with column observations from the Total Carbon Column Observing Network (TCCON) and the Greenhouse

1

Gases Observing Satellite (GOSAT) show that OCO-2 observations can be used reliably to estimate IAV. Furthermore, the extensive spatial coverage of the OCO-2 satellite data leads to smoother IAV timeseries than those from other datasets, suggesting that OCO-2 provides new capabilities for revealing small IAV signals despite sources of noise and error that are inherent to remote sensing datasets.

1 Introduction

Increasing atmospheric CO_2 concentration from anthropogenic emissions is the major driver of the observed warming of Earth's climate since the industrial revolution (IPCC, 2021). Although CO_2 accumulation in the atmosphere generally is ~45% of anthropogenic emissions on a multi-year average (Ciais et al., 2013; Friedlingstein et al., 2019), the growth rate shows substantial interannual variability (Conway et al., 1994). The difference between emissions and the atmospheric CO_2 growth rate results from net CO_2 uptake by oceans and terrestrial ecosystems (Prentice et al., 2001; Doney et al., 2009), and the fluctuations reflect variations in the strength of those sinks due to climate variations (Peters et al., 2017; Friedlingstein et al., 2019). Much research has suggested that interannual variability (IAV) in the growth rate is predominantly due to variations in terrestrial ecosystem carbon uptake (Marcolla et al., 2017), even though the average uptake is roughly comparable between land and ocean (Le Quéré et al., 2009). Existing atmospheric CO_2 observations from surface flask sampling and in situ networks have been used to estimate global- and regional-scale interannual variability in CO_2 fluxes (Gurney et al., 2008; Peylin et al., 2013; Keppel-Aleks et al., 2014; Piao et al., 2020). We note, however, that the surface observing network is located primarily on land and coastal sites, and more subtle ocean flux signals may be obscured by the large IAV in terrestrial fluxes.

Previous analyses of surface CO_2 IAV has shown a strong relationship with the phase and intensity of El Niño–Southern Oscillation (ENSO) (Le Quéré et al., 2009; Schwalm et al., 2011). ENSO variations originate from coupled ocean-atmosphere dynamics that are reflected in large wind and sea surface temperature anomalies over the central and eastern Pacific Ocean. ENSO affects the climate of much of the tropics and subtropics via atmospheric teleconnections on timescales of 2-7 years (Timmermann et al., 2018). On land, suppressed precipitation and high temperature associated with positive phases of ENSO (El Niño conditions) suppress CO_2 uptake by tropical ecosystems, while promoting fires that further reduce the CO_2 uptake by lands (Feely et al., 2002; McKinley et al., 2004; Piao et al., 2009; Wang et al., 2014). Although of smaller magnitude, the equatorial Pacific Ocean experiences weakening of the easterly trade winds and suppression of ventilation of deep, cold, carbon-rich waters to the surface during an El Niño, reducing the efflux of natural CO_2 to the atmosphere (Patra et al., 2005 ; Chatterjee et al., 2017).

Chatterjee et al. (2017) were able to directly observe the ocean flux-driven signal on atmospheric CO_2 from El Niño for the first-time using XCO_2 (column-averaged dry air CO_2 mole fraction) observed over the ocean by NASA's OCO-2 satellite. Space-based observations from OCO-2, which launched in July 2014, provide novel opportunities to characterize the patterns of IAV in XCO_2 in areas that were previously not directly observed by existing monitoring networks. The IAV in XCO_2 is being used implicitly for flux attribution in inverse modeling studies (Nassar et. al,

2011). These exciting results, however, must be tempered by an awareness that atmospheric CO_2 IAV is a relatively small signal. For example, IAV in the surface network is about 1 ppm in scale compared to a seasonal amplitude of around 10 ppm in northern high latitudes. OCO-2 measures column averaged CO_2, so its measurements are sensitive to variations in the boundary layer mole fraction, which is in direct contact with the land or atmospheric fluxes, but also variations in the free troposphere and stratosphere, where flux signals are generally smaller than those observed at the surface (Olsen and Randerson, 2004). Furthermore, variations in the free troposphere are expected to have relatively long correlation length scales due to efficient mixing, making it important to consider the spatial scales at which XCO_2 observations provide unique information. This is especially important in light of analysis which suggests that the error variance budget in OCO-2 observations is large and contains substantial spatially coherent signal (Baker et al., 2022; Torres et al., 2019; Mitchell et al., 2023).

In this paper, we analyze XCO_2 from OCO-2 to characterize spatiotemporal patterns in IAV at near-global scale, over both land and ocean, and relate XCO_2 variations to ENSO conditions. We contextualize the information contained in OCO-2 observations by comparing with space-based GOSAT and ground-based TCCON XCO_2 and with surface measurements of CO_2. Finally, we use these comparisons to emphasize the spatial scales at which the IAV signal emerges from instrumental noise.

2 Data and Methods

2.1 Datasets

2.1.1 OCO-2 observatory

We analyzed IAV in dry air, column-average mole fraction XCO_2 inferred from OCO-2 satellite observations. The OCO-2 observatory was launched in July 2014 and has measured passive, reflected solar near infrared CO_2 and O_2 absorption spectra using grating spectrometers since September 2014 (Eldering et al., 2017). XCO_2 data are retrieved from the measured spectra using the Atmospheric CO_2 Observations from Space (ACOS) optimal estimation algorithm, which is a full physics algorithm that takes into account XCO_2 and other physical parameters, including surface pressure, surface albedo, temperature, and water vapor profile in its state vector (O'Dell et al., 2018). The satellite flies in a polar and sun-synchronous orbit that repeats every 16 days, with three different observing modes of OCO-2, namely nadir (land only, views the ground directly below the spacecraft), glint (over ocean and land, views just off the peak of the specularly reflected sunlight), and target (typically for comparison with specific ground-based or airborne measurements) (Crisp et al., 2012; Crisp et al., 2017). We use the version 10 OCO-2 Level 2 bias-corrected XCO_2 data product from Goddard Earth Sciences Data and Information Services Center (GES DISC) Archive: https://disc.gsfc.nasa.gov/datasets/OCO2_L2_Lite_FP_10r/summary), which has been validated with collocated ground-based measurements from the Total Carbon Column Observing Network (TCCON; discussed in more detail in Section 2.2). After filtering and bias correction, the OCO-2 XCO_2 retrievals agree well with TCCON in nadir, glint, and target observation modes, and generally have absolute median differences less than 0.4 ppm and Root Mean Square differences less than 1.5 ppm (O'Dell et al., 2018; Wunch et al., 2017).

2.1.2 TCCON

We corroborate patterns of XCO$_2$ IAV from OCO-2 with those from TCCON, a ground-based network of Fourier transform spectrometers that measure direct solar absorption spectra in the near infrared (Wunch et al., 2011).
Retrievals of XCO$_2$ and other gases are computed using the GGG algorithm, a nonlinear least-squares spectral fitting algorithm. The TCCON retrievals are tied to the World Meteorological Organization (WMO) X2007 CO$_2$ scale via calibration with aircraft and AirCore profiles above the TCCON sites (Karion et al., 2010; Wunch et al., 2010). This ensures an accuracy and precision of ~0.6 ppm (1-sigma) throughout the network (Washenfelder et al., 2006; Messerschmidt et al., 2010; Deutscher et al., 2010, Wunch et al., 2010). TCCON has been used widely as a validation standard by providing independent measurements to compare with multiple satellite XCO$_2$ retrievals including OCO-2. In previous work Sussmann and Rettinger (2020) have demonstrated a concept to retrieve annual growth rates of XCO$_2$ from TCCON data, which are regionally to hemispherically representative in spite of the non-uniform sampling in time and space inherent to the ground-based network. In our study, we focus on IAV in the XCO$_2$ timeseries from 26 TCCON sites (Table 1, Fig.1) that have at least 3 years of observational coverage within the period from September 2014 to June 2021. These TCCON data have been filtered using the standard filter that is based on a measure of cloudiness and limits the solar zenith angle. Data are publicly available from the TCCON GGG2014 Data Archive (https://tccondata.org/) hosted by the California Institute of Technology.

Table 1. TCCON Column-Averaged Dry-Air Mole Fractions of CO$_2$ (GGG2014 Data)

Region	Site	Acronym	Latitude	Longitude	Start Date	End Date	Publication
Polar Northern Hemisphere (60-90°N)	Eureka (NU)	eu	80.05	-86.42	2010-07	2020-07	Strong, K. et al., 2017
	Ny Ålesund	sp	78.90	11.90	2014-04	2019-09	Notholt, J. et al., 2019
	Sodankylä (FI)	so	67.37	26.63	2009-05	2020-10	Kivi, R. et al., 2017
Temperate Northern Hemisphere (20-60°N)	East Trout Lake(SK)	et	54.35	-104.99	2016-10	2020-09	Wunch, D., et al., 2017
	Bialystok (PL)	bi	53.23	23.03	2009-03	2018-10	Deutscher, N. et al., 2017
	Bremen (DE)	br	53.10	8.85	2010-01	2020-06	Notholt, J. et al., 2017
	Karlsruhe (DE)	ka	49.10	8.44	2010-04	2020-11	Hase, F. et al., 2017
	Paris (FR)	pr	48.97	2.37	2014-09	2020-06	Te, Y. et al., 2017
	Orléans (FR)	or	47.97	2.11	2009-08	2020-06	Warneke, T. et al., 2017
	Garmisch (DE)	gm	47.48	11.06	2007-07	2020-06	Sussmann, R. et al., 2017
	Zugspitze (DE)	zs	47.42	10.98	2015-04	2020-06	Sussmann, R. et al., 2018
	Park Falls (US)	pa	45.95	-90.27	2004-06	2020-12	Wennberg, P. O. et al., 2017
	Rikubetsu (JP)	rj	43.46	143.77	2013-11	2019-09	Morino, I. et al., 2017
	Lamont (US)	oc	36.60	-97.49	2008-07	2020-12	Wennberg, P. O. et al., 2017
	Anmyeondo (KR)	an	36.58	126.33	2015-02	2018-04	Goo, T.-Y. et al., 2017
	Tsukuba (JP)	tk	36.05	140.12	2011-08	2019-09	Morino, I. et al., 2017
	Edwards (US)	df	34.96	-117.88	2013-07	2020-12	Iraci, L. et al., 2017
	Caltech (US)	ci	34.14	-118.13	2012-09	2020-12	Wennberg, P. O. et al., 2017
	Saga (JP)	js	33.24	130.29	2011-07	2020-12	Shiomi, K.et al., 2017
	Izana (ES)	iz	28.30	-16.50	2007-05	2021-02	Blumenstock, T. et al., 2017

Tropical Northern Hemisphere (0-20°N)	Burgos (PH)	bu	18.53	120.65	2017-03	2020-03	Morino, I., et al., 2018
Tropical Southern Hemisphere (0-20°S)	Ascension Island (SH)	ae	-7.92	-14.33	2012-05	2018-10	Feist, D. G. et al., 2017
	Darwin (AU)	db	-12.46	130.94	2005-08	2020-04	Griffith, D. W. T., et al., 2017
Temperate Southern Hemisphere (20-60°S)	Réunion Island (RE)	ra	-20.90	55.49	2011-09	2020-07	De Maziere, M. et al., 2017
	Wollongong (AU)	wg	-34.41	150.88	2008-06	2020-06	Griffith, D. W. T. et al., 2017
	Lauder (NZ)	ll	-45.04	169.68	2010-02	2018-10	Sherlock, V. et al., 2017
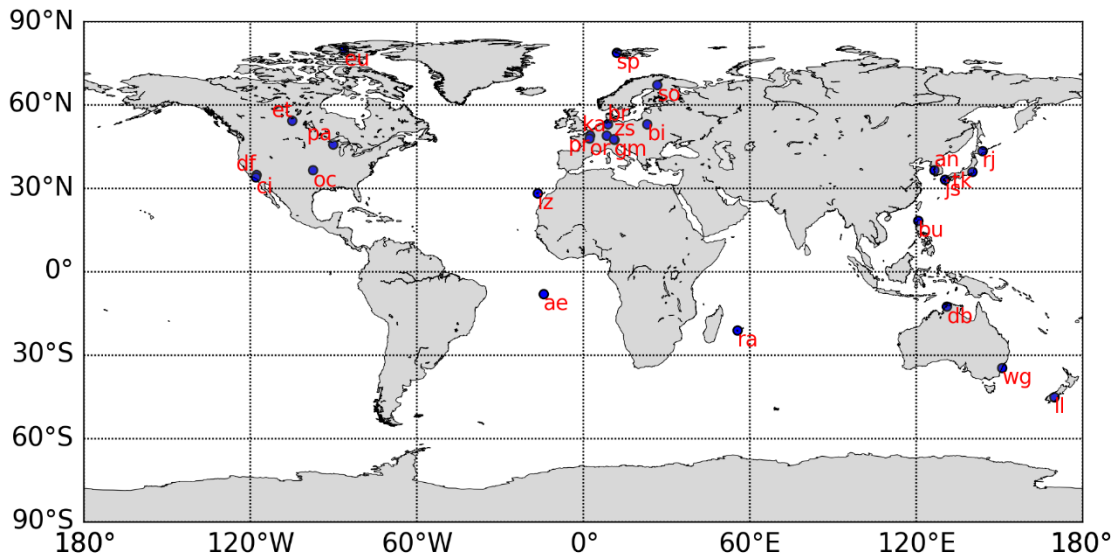
Figure 1. Map showing the locations and the acronyms of the TCCON sites.

2.1.3 Marine Boundary Layer Observations

To explore differences in surface and column-average CO_2 IAV, we analyze IAV in the surface CO_2 mole fraction at marine boundary layer (MBL) sites in the NOAA (National Oceanic and Atmospheric Administration) cooperative sampling network(https://gml.noaa.gov/dv/site/?program=ccgg). At these sites, boundary layer CO_2 is measured using weekly flask samples (Masarie and Tans, 1995; Dlugokencky et al., 2021). MBL sites are typically far away from anthropogenic sources and regions of active terrestrial exchange, so they provide an estimate for large-scale patterns in the global background CO_2 concentration. The surface MBL dry air mole fraction data has an accuracy level of about 0.1 ppm. In this study, we select 16 sites with at least 80% data coverage for the approximately 7-year period overlapping with OCO-2 (Table 2, Fig.2), and the data are aggregated into four north-south zones for comparison with OCO-2 XCO_2: northern and southern hemisphere tropical (0 - 20°) and Northern Hemisphere/Southern Hemisphere extratropical zones (20-60°). Each belt contains at least three MBL sites. Higher

latitudes (60-90°) are not considered in this comparison due to the gaps remaining in the OCO-2 XCO_2 record in high latitudes during wintertime and shouldering seasons.

Table 2. Marine Boundary Layer stations within the NOAA Earth System Research Laboratory CO_2 sampling network

| Region	Station	Acronym	Latitude	Longitude	Start Date	End Date
Temperate Northern Hemisphere (20-60°N)	Mace Head, Ireland	MHD	53.3	-9.9	2014-01	2020-07
	Shemya, AK	SHM	52.7	174.1	2014-01	2020-07
	Terceira Island Azores	AZR	38.8	-27.4	2014-01	2020-07
	Tudor Hill, Bermuda	BMW	32.3	-64.9	2014-01	2020-07
	Sand Island, Midway	MID	28.2	-177.4	2014-01	2020-07
	Key Biscayne, FL	KEY	25.7	-80.2	2014-01	2020-07
Tropical Northern Hemisphere (0-20°N)	Cape Kumukahi, HI	KUM	19.5	-154.8	2014-01	2020-07
	Mariana Islands, Guam	GMI	13.5	144.7	2014-01	2019-08
	Ragged Pointed, Barbados	RPB	13.2	-59.4	2014-01	2020-07
	Christmas Island, Republic of Kiribati	CHR	1.7	157.2	2014-01	2019-08
Tropical Southern Hemisphere (0-20°S)	Seychelles	SEY	-4.7	55.2	2014-01	2020-07
	Ascension Island	ASC	-8.0	-14.4	2014-01	2020-07
	Tutuila, America Samoa	SMO	-14.2	-170.6	2014-01	2020-07
Temperate Southern Hemisphere (20-60°S)	Cape Grim, Australia	CGO	-40.7	144.7	2014-01	2020-07
	Baring Head	BHD	-41.4	174.9	2014-01	2020-07
	Crozet Island	CRZ	-46.5	51.9	2014-01	2020-07
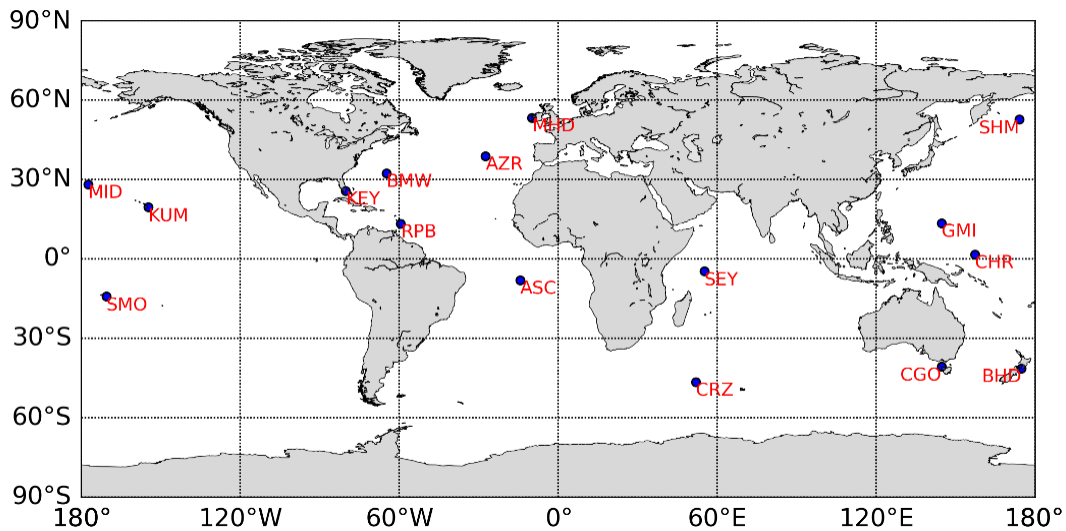
Figure 2. Map showing the locations and the acronyms of the Marine Boundary Layer stations within the NOAA Earth System Research Laboratory CO_2 sampling network.

2.1.4 GOSAT

We compare patterns of XCO_2 IAV from OCO-2 with those from GOSAT. Also known as Ibuki, GOSAT is the world's first satellite dedicated to greenhouse gas monitoring, measuring global total column CO_2 and CH_4 since 2009.

With the Thermal and Near infrared Sensor for carbon Observation (TANSO) - Fourier Transform Spectrometer (FTS) onboard for greenhouse gas monitoring using three SWIR bands and one TIR band (Cogan et al., 2012; Yoshida et al., 2013). Column-averaged dry mole fraction are obtained at a circular footprint of approximately 10.5 km. GOSAT has a regional biased of about approximately 0.3 ppm and 1.7 ppm single observation error versus the TCCON (Kulawik et al., 2016). We utilize the FTS SWIR Level 3 data global monthly 2.5° resolution mean CO_2 mixing ratio products from 2009 June to 2021 December to generate IAV and make comparisons with OCO-2. L3 products are generated by interpolating, extrapolating, and smoothing the FTS SWIR column-averaged mixing ratios of CO_2 and apply the geostatistical calculation technique Kriging method. GOSAT observation datasets are available to public at NIES GOSAT website (https://www.gosat.nies.go.jp/en/about_5_products.html).

2.1.5 Multivariate ENSO Index (MEI)

We use the bi-monthly Multivariate El Niño/Southern Oscillation (ENSO) index (MEI; downloaded from Physical Sciences Laboratory: https://psl.noaa.gov/enso/mei/) to explore the relationship between CO_2 IAV and ENSO. The MEI is the time series of the leading combined Empirical Orthogonal Function of five different variables (sea level pressure, sea surface temperature, zonal and meridional components of the surface wind, and outgoing longwave radiation) over the tropical Pacific basin. Positive values in the MEI indicate El Niño conditions, while negative values indicate La Niña conditions, and the magnitude reflects the relative strength. Unlike other ENSO indices which use only one climate metric (e.g., the sea level pressure difference between Tahiti and Darwin or the sea surface temperature anomaly within a pre-defined box), the MEI provides for a more complete and flexible description of the ENSO phenomenon than traditional single variable ENSO indices and has less vulnerability to errors (Klaus Wolter et. al, 2011).

2.2 Methods

2.2.1 Spatial Aggregation

We aggregate daily XCO_2 observations from the version 10 OCO-2 Level 2 lite product to monthly scale, exploring patterns of IAV at three spatial scales: gridcell-level, zonal averages over 5° of latitude, and broad zonal belts. Aggregating soundings reduces random noise in the observations, mitigates the impact of data gaps due to cloud cover, and partly mitigates effect from low winter sunlight levels in polar regions. For gridcell level analysis, we aggregate data equatorward of 45° to 5°x5° bins since these data are not limited by polar night or degraded by high solar zenith angles during winter. Poleward of 45° in both hemispheres, we aggregate the satellite observation to a latitude-longitude resolution of 5°x10° to compensate for fewer and noisier soundings in these latitudes, especially during winter and its shoulder seasons. Within each 5°x5° or 5°x10° gridcell, only months that have more than 5 soundings are included in the analysis. Our criteria for aggregation are based on sensitivity experiments in which we modulated the grid cell resolution from 1°x1° to 15°x15° (Fig. S1 and Fig. S2) and varied the threshold on the required number of soundings within a month from 1 to 25 (Fig. S3, Fig. S4 and Fig. S5). Our goal was to reduce noise but maintain high spatial coverage (Fig. S6 and Fig. S7). The 5°x5° and 5°x10° aggregation strike the necessary balance of reducing

noise (evidenced by the smoother IAV amplitude fields as aggregation increases in Fig. S1) but maintaining spatial information by not oversmoothing (evidenced by the fact that the aggregation occurs at spatial scales finer than the "elbow" where correlations among 1° gridcells stop changing with separation distance in Fig. S8)

In our analysis, we also aggregate data to zonal averages. At intermediate spatial scales, we average all data around the 5° latitude bins described above. For comparison with TCCON and MBL data, which are spatially sparse, we further aggregate XCO_2 data into four broad zonal belts – each of which contains at least 1 TCCON or 3 MBL stations -- (delineated in Table.1 and Table.2) to assess IAV patterns among the datasets. Keppel-Aleks et al., (2014) showed that drivers of IAV (i.e., temperature, drought stress, or fire) could be attributed when surface CO_2 were aggregated into similar broad zonal belts, whereas process-level attribution was not possible with global averaging. We therefore analyze broad zonal belts to gain a large-scale understanding of how three CO_2 datasets are similar and where differences lie.

2.2.2 Deriving interannual variations

We use a consistent process to calculate IAV (Equation 1) from the raw OCO-2, TCCON and MBL timeseries. The methodology is based on approaches used in Keppel-Aleks et al. (2013) and NOAA curve fitting methodology (Thoning et al, 1989). We decompose the raw time-series data into a long-term trend (which is a function of location (x,y) and time (t)), a seasonal cycle (which is a function of location and calendar month (m)), and IAV anomalies using Equation 1:

$$IAV(x,y,t) = Raw(x,y,t) - Trend(x,y,t) - Seasonal(x,y,m) \qquad \text{Equation 1}$$

We first fit a third order polynomial to the Raw timeseries to calculate the observed trend at each location (Fig. 3a). After removing the trend calculated at each gridcell (Fig. 3b), we calculate a mean seasonal cycle by taking the mean value of all January, February, etc. data (Fig. 3c). Particularly at high latitudes, some months are systematically under sampled. For these gridcells, we must have at least two years with sufficient observations to calculate a climatological mean for that month, otherwise, that calendar month is assumed to have insufficient data to infer the IAV. Finally, we remove the mean seasonal cycle from the detrended timeseries at each gridcell to obtain the IAV anomaly timeseries (Fig. 3d). Given the short data record, we quantify the uncertainty in our calculation of the climatological seasonal cycle as the standard error for each calendar month (blue shading in Fig. 3c), and this uncertainty is propagated to the corresponding IAV timeseries (Fig. 3d). We fit a third order polynomial to the raw timeseries since the GOSAT,MBL and TCCON timeseries extend over a decade in length. We confirm that the use of a third-order polynomial, versus a second-order polynomial, does not remove the IAV signal from the shorter OCO-2 timeseries (Fig. S9).
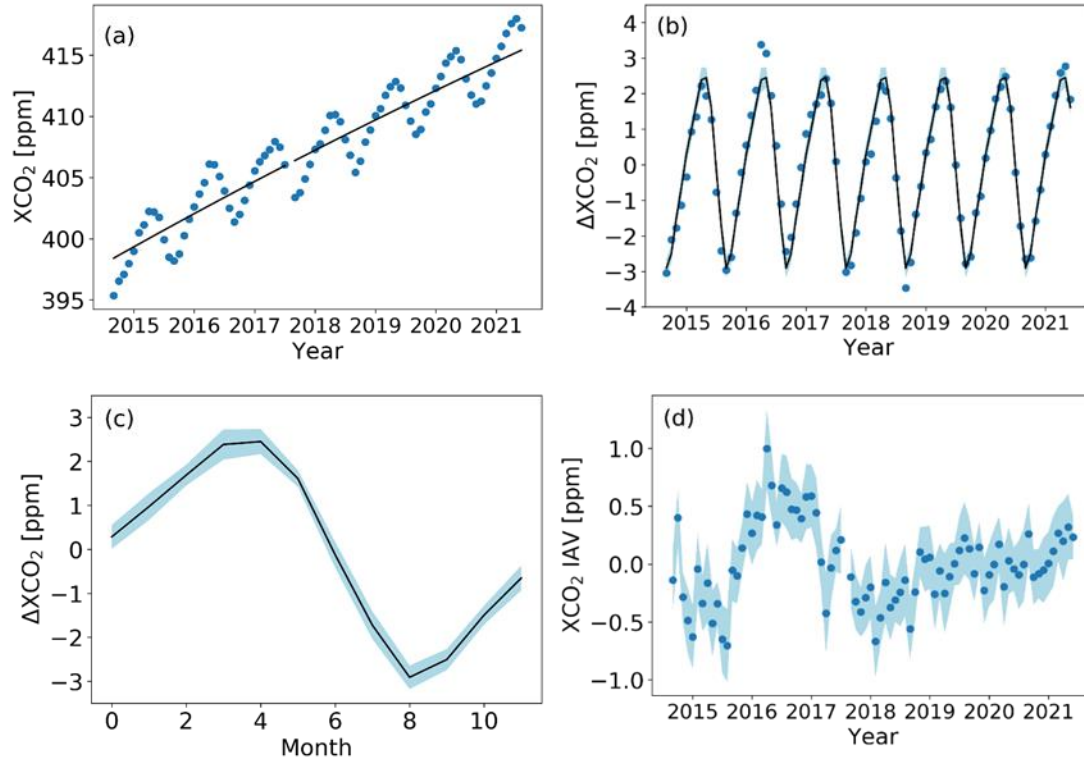
8

Figure 3. Methodology to calculate the CO_2 interannual variability timeseries, using OCO-2 XCO_2 data at the 5° grid cell at 20°N, 155°W, which contains Moana Loa, as an example. (a) 5°resolution monthly mean raw OCO-2 XCO_2 and the associated 3rd order polynomial trend. (b) detrended monthly XCO_2 after removing the long-term trend with a repeating 12-month annual cycle obtained from calculating the mean for each month. The light blue shading gives the uncertainty of the seasonal cycle, which is derived by calculating the standard deviation across all Januarys, Februarys, etc. (c) 12-month mean annual cycle together with the uncertainty range plotted in (b). (d) Resulting interannual variability, when mean annual cycle is removed from detrended timeseries.

3 Results

3.1 Spatiotemporal Variations based on OCO-2 observation

When averaged into broad zonal belts representing the tropics and mid-latitudes, the OCO-2 XCO_2 IAV timeseries anomalies range between -0.5 to 0.75 ppm (Fig. 4a). All latitude bands show increasing IAV during positive MEI (El Niño) and decreasing IAV during negative MEI (La Niña), although the phasing varies among latitudes. During the strong 2015–2016 El Niño, which began around March 2015 and reached its peak at the start of 2016, XCO_2 showed the largest IAV. The Southern Hemisphere extratropical region (Fig. 4d) have larger and more rapid response in the IAV associated with ENSO compared to other zones, especially for the smaller El Niño that peaked at the beginning of 2020. At this time, the XCO_2 IAV timeseries (Fig. 4d) had an anomaly nearly twice as large as that of other latitude belts (Fig. 4a to 4c). During both El Niño events, the IAV timeseries in the NH tropics zone peaks nearly six months after the maximum MEI value.

9

290   We assess the spatial correlation patterns with no time lag, 3-month, 6-month lag between the IAV timeseries and MEI (Fig. 8a). The XCO₂ IAV timeseries have strong correlation coefficient with the MEI index in both Southern Hemisphere and Northern Hemisphere low latitudes from 0° to 30°N at lag 0, whereas in the Northern Hemisphere extratropics, the maximum positive correlation occurs at month 4 (Fig. 8b). The positive correlation between MEI and the IAV timeseries is gradually attenuated, with no clear correlation at six months lag (Fig. 8c).

295
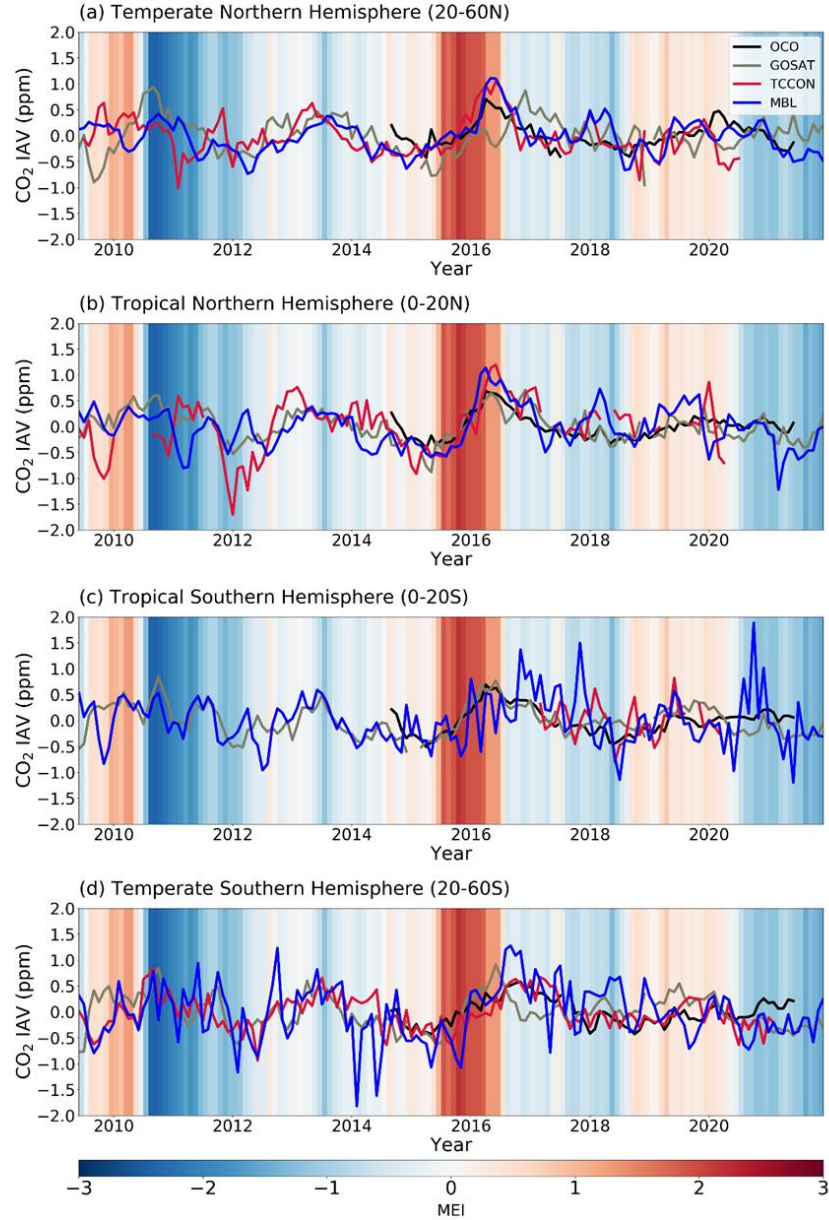
Figure 4. IAV timeseries averaged for zonal bands between 60 °N and 60 °S from four different observing strategies: Space-based OCO-2 XCO₂ (Black), Surface CO₂ observations from NOAA's marine boundary layer (MBL) sites (Blue), Ground-based TCCON XCO₂ (Red), Space-based GOSAT XCO₂ (Gray). (a) temperate northern hemisphere (20°N-60°N), (b) tropical northern hemisphere (0° - 20°N), (c) tropical southern hemisphere (0°-20°S), (d) temperate southern hemisphere (20°S-60°S). For all panels, the background shading indicates the Multivariate ENSO Index (MEI), which is positive during El Niño phases.

10

The differences in temporal phasing between the broad zonal belts (Fig. 4a) associated with El Niño events can be linked to transport of El Niño-driven CO_2 flux anomalies away from the tropics when zonal means are calculated from OCO-2 observations at 5° latitude resolution (Fig. 5). For the two El Niño periods in 2015-2017 and late-2018 to 2021, high IAV values originate in the tropics and a smooth transition to high IAV values is seen at higher latitudes as time progresses (Fig. 5a). We note that fluxes outside the tropics may also be influenced by ENSO-related climate variability, yet the transport of tropical-driven anomalies appears to dominate. This 7-year study period also captures the half-year lags for atmospheric transport or climate-ecological teleconnections that impacts XCO_2 variations in the far North. While the OCO-2 patterns largely conform with variability expected based on ENSO and are in broad agreement with other observational networks, there are some anomalies that cannot be explained, such as the high XCO_2 in early 2020 around 60°S (Fig. 5a). Even with more aggressive data filtering, this episode persists, requiring more investigation of unknown geophysical drivers of high XCO_2 or potential retrieval issues that could cause a high bias.
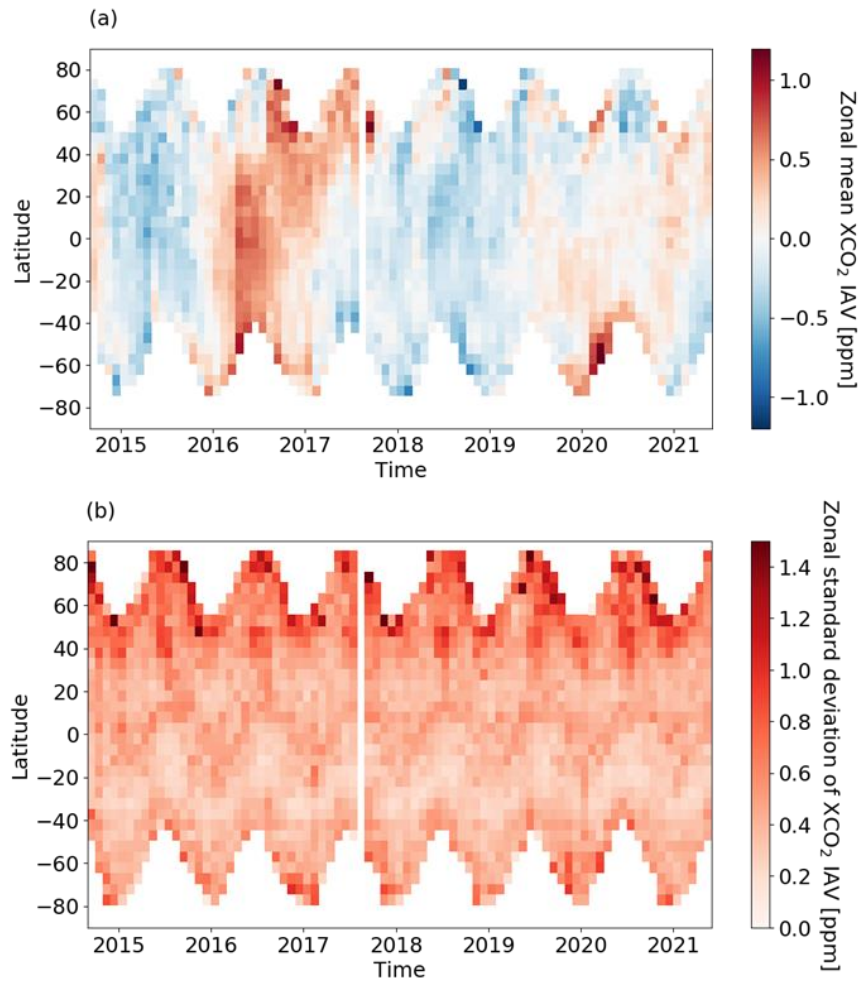
Figure 5. Hovmöller Diagrams diagram showing zonal mean OCO-2 XCO_2 IAV timeseries for 5° latitude bins (a) and the zonal standard deviation of XCO_2 IAV (b), which gives an estimate of coherence in the IAV patterns among grid cells in the 5° zonal belt.

11

We quantify coherence in CO_2 IAV within a latitude circle by taking the standard deviation across gridcell-level IAV anomalies within each 5° latitude zone. The standard deviation among gridcells is highest in the far North, with values as high as 1 ppm poleward of 45°N and as low as 0.2 ppm in the Southern Tropical bands (Fig. 5b), indicating that IAV is less spatially coherent in the Northern Hemisphere. This may be consistent with studies that show greater IAV in terrestrial ecosystem fluxes (concentrated in the northern hemisphere) (Zeng et al., 2005) relative to ocean fluxes, or may reflect that our IAV timeseries also retains the imprint of sampling, measurement, and retrieval errors, which become more pronounced at higher latitudes. In general, there is not a time-dependent or ENSO-related pattern for the longitudinal variation of IAVs (no obvious changes during the two El Niño periods), which suggests the variation within each 5° band may be approximately stable and does not change substantially with interannual climate events.
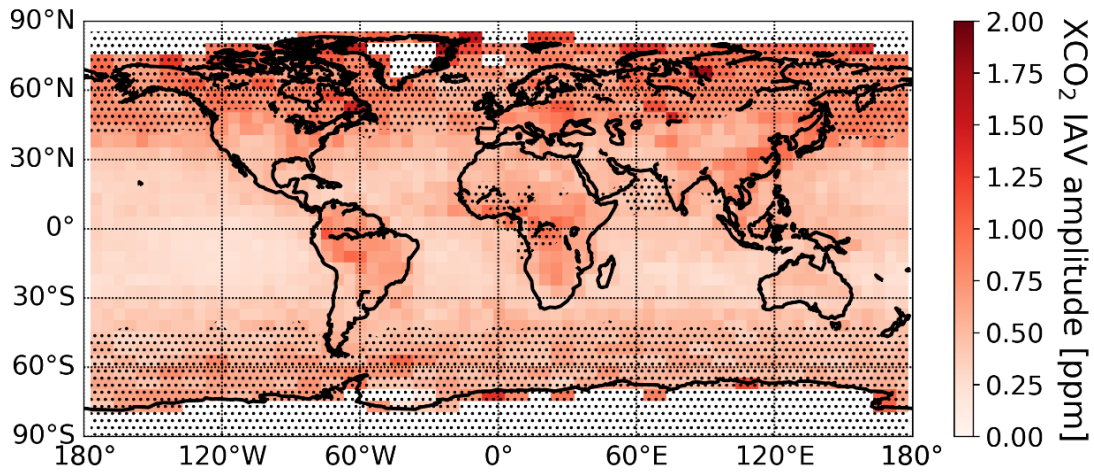
Figure 6. OCO-2 XCO₂ IAV amplitude, determined as the standard deviation of the IAV timeseries. Data equatorward of 45° are averaged at 5°by 5° resolution , and data poleward of 45° are averaged at 5°by 10° resolution. Shaded regions indicate gridcells that lack mean annual cycle data for at least two calendar months due to polar night or related retrieval challenges.
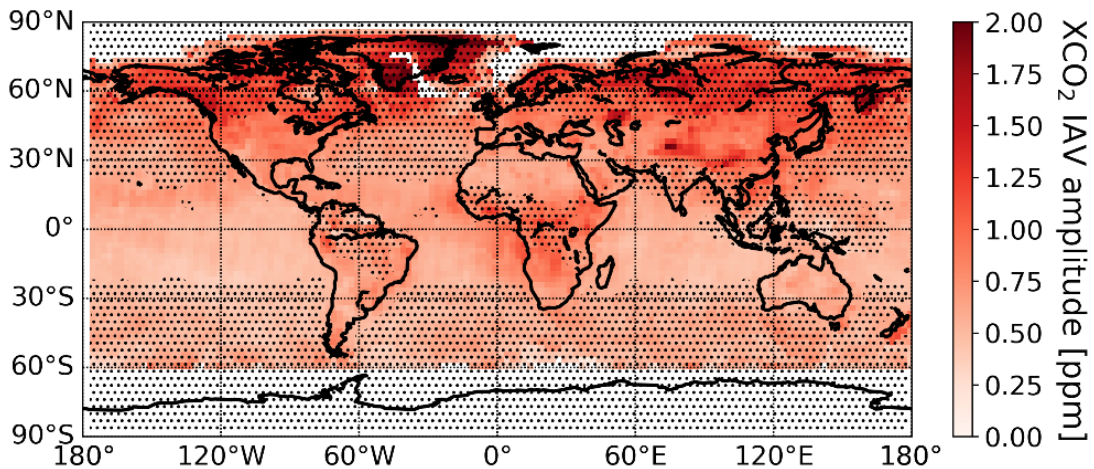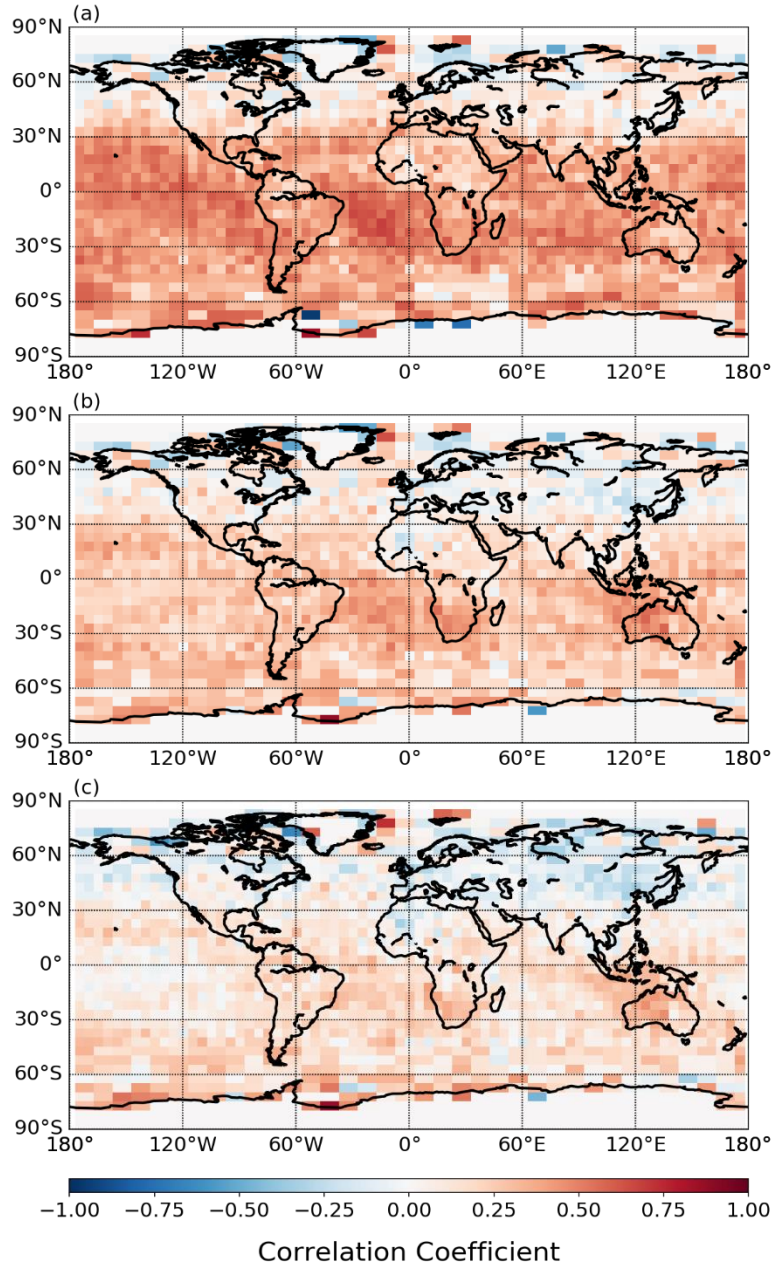

Figure 7. Similar as Figure 6 but based on GOSAT data.

Figure 8. Correlation coefficient between local grid cell OCO-2 XCO$_2$ IAV timeseries and MEI, for (a) synchronous timeseries, (b) with 3-month lags, (c) with 6-month lags.

The XCO$_2$ IAV amplitude (the standard deviation of the IAV timeseries) is notably larger over continental gridcells compared to ocean gridcells (Fig. 6). In both hemispheres, the IAV amplitude over subtropical ocean basins is less than 0.4 ppm, while the IAV amplitude over tropical land in Southeast Asia, Congo forests and Amazon Basin is about 1 ppm. In higher latitudes, the XCO$_2$ IAV amplitude can exceed 1.2 ppm above deciduous and boreal forests in North America and Eurasia. Higher values over land likely occur due to the active CO$_2$ exchange between terrestrial ecosystem and the atmosphere, but we cannot rule out that retrievals over land show more variance due to complex topography, albedo, etc., which are elements of the retrieval state vector. Nevertheless, over land areas with low carbon

13

exchange (e.g., Australia, the Middle East, the Sahara Desert), the XCO_2 IAV amplitude is nearly of the same low level as the ocean basins. It is worth noting that for high latitude regions, including both Northern continents and Southern Ocean, OCO-2 does not obtain observations over a full calendar year (stippled gridcells in Fig. 6) due to polar nights, low light levels, and high solar zenith angles. The XCO_2 IAV amplitudes are less zonally coherent
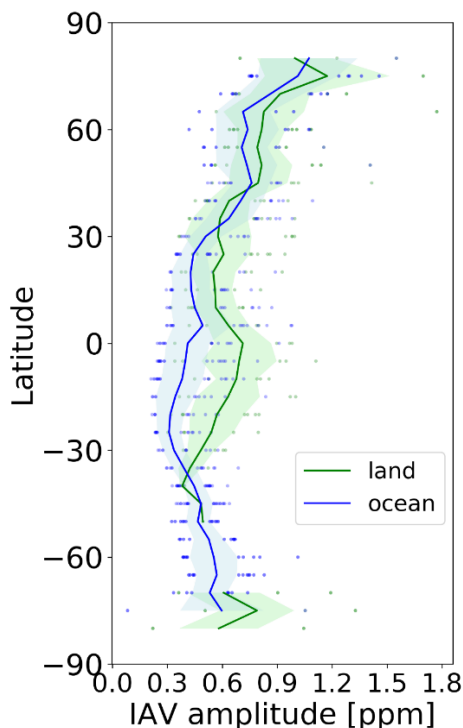

380

Figure 9. Latitudinal profile for zonal mean of IAV amplitude and the standard deviation among land (green) or ocean (blue) gridcells in each latitude band (shaded area). Individual points represent all grid cells valid IAV record within the certain zonal band.
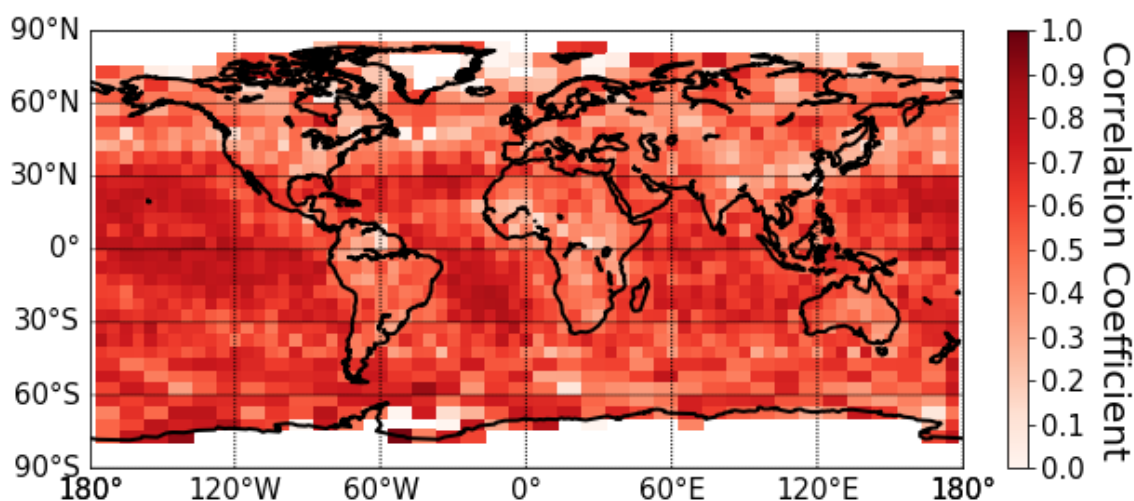
385   **Figure 10. Correlation coefficient between local grid cell IAV timeseries and the corresponding 5° zonal mean OCO-2 XCO_2 IAV timeseries.**

through these regions than those in the tropics and mid-latitudes, for both land and ocean. When averaging all ocean or land grid cells around a latitude circle, the zonal mean IAV amplitude over the ocean ranges from 0.3 to 1.0 ppm, while the land IAV amplitude ranges from 0.4 to 1.1 ppm (Fig. 9). Both the land and ocean profiles have similar north-south patterns, with higher IAV amplitude in the Northern Hemisphere and lower IAV amplitude in the Southern Hemisphere, and the small IAV amplitudes in the subtropics of both hemispheres, with more scatter among land gridcells than ocean (Fig. 5b and Fig. 9), suggesting either the influence of local flux IAV on land or greater error associated with retrievals on land. We note better coherence between the XCO_2 IAV timeseries of each local grid cell and that of zonal mean XCO_2 IAV timeseries for ocean, with correlation coefficients of approximately 0.8. In contrast, land gridcells are generally correlated with the zonal mean at around 0.4 to 0.6 (Fig. 10).

3.2 OCO-2 XCO_2 IAV compared to GOSAT XCO_2 IAV

We carried out comparisons between the global spatiotemporal pattern of XCO_2 IAV between OCO-2 and GOSAT, since GOSAT has data beginning in 2009. The XCO_2 timeseries from OCO-2 provides higher coverage over mid-latitude oceans and tropical rainforests (stippling in Fig. 6, 7). The IAV amplitude of OCO-2 is generally smaller than that of GOSAT worldwide (Fig. 6, 7), which may be due to greater data volume and reduced noise in the OCO-2 dataset (Wu et al., 2020). OCO-2 and GOSAT zonal mean IAV timeseries generally share the same feature from 2014 to 2021 (Fig. 4a-d), with an increasing trend during El Niño and decreasing trend during La Niña, however the GOSAT XCO_2 shows a delayed response in the northern midlatitudes, by almost 9 months, to the strong 2015 El Niño compared to the other datasets. Generally, GOSAT IAV timeseries are nosier, from month-to-month, compared to those from OCO-2.

3.3 XCO_2 IAV compared to surface and TCCON ground-based sites

Given that the small IAV signal (up to 1 ppm over land, and smaller over ocean) is similar in magnitude to noise and systematic bias in OCO-2 soundings (Torres et al., 2019), we corroborate patterns of IAV from OCO-2 with other datasets. The OCO-2 IAV timeseries in broad latitudinal belts share similarities with those of TCCON XCO_2 and MBL surface CO_2 ground-based IAV timeseries, with all timeseries showing similar relationships to MEI. Especially striking is that all timeseries capture the lagged response in the NH midlatitude belt to the strong 2015/16 El Niño (Fig. 4a-d). Although the patterns are similar, the magnitude of IAV at the MBL sites is almost double the IAV in the OCO-2 XCO_2 timeseries. Given that the atmospheric boundary layer, where surface observations are made, is on average 10% of the total column, this suggests that much IAV in total column observations is present within the free troposphere. For TCCON, the amplitude of IAV is similar to that of OCO-2, since both methods capture total column variations. We note that the zonal IAV timeseries for MBL and TCCON appear to have more high frequency variations than those from OCO-2 (Fig. S10, Fig. S11 & Fig. S12), which likely stems from the fact that the zonal composites are developed from sparse ground-based sites (between 1 and 12 observatories) within each latitude belt, whereas the satellite measures at all longitudes within a belt, though with more limited time resolution. The zonal mean OCO-2 observations are correlated with MBL sites within the same latitude band with R between 0.5 and 0.75 (diagonal elements on Fig. 13b). Correlations between zonal TCCON and OCO-2 observations range between 0.15 and 0.55

(Table. S1). The correlations are weakest in the northern tropics band, where TCCON data were unavailable during
425 the strong El Niño (Fig. 3c). It is noteworthy that OCO-2 zonal averages are more correlated among different latitudes
than are MBL or TCCON observations (off-diagonal elements in Fig. 13c, d, e). The greater correlation across latitudes
for OCO-2 compared to MBL sites is likely due to the sensitivity of the OCO-2 XCO_2 observations to the free
troposphere, where meridional transport is more rapid than at the surface. While TCCON data are also sensitive to the
free troposphere, we hypothesize that the zonal belt averages for TCCON, constructed from only a few sites, are more
430 affected by noise, both instrumental and geophysical, and thus show lower coherence than the OCO-2 XCO_2 averages
constructed from the whole latitudinal bands.

We further compared the IAV from OCO-2 XCO_2 with TCCON stations at the site level (Fig. 12). Across all sites,
the IAV amplitude generally shows good agreement and lies between 0.4 to 1.2 ppm. We note a slight low IAV
435 amplitude in OCO-2 relative to TCCON for all five sites in the Southern Hemisphere which lie below the one-to-one
line. Low OCO-2 IAV amplitudes may be due to the fact that a 5x5 ° gridcell encompassing these near-coastal
locations includes both land and ocean OCO-2 soundings, and may be due to specific sources of variance from retrieval
bias affected by surface type for the OCO-2 (e.g., Fig. 9). It is also worth noting that OCO-2 is looking at a region of
5° by 5° gridcell (or 5° by 10° in higher latitudes) around TCCON sites, so there are different signals affecting the
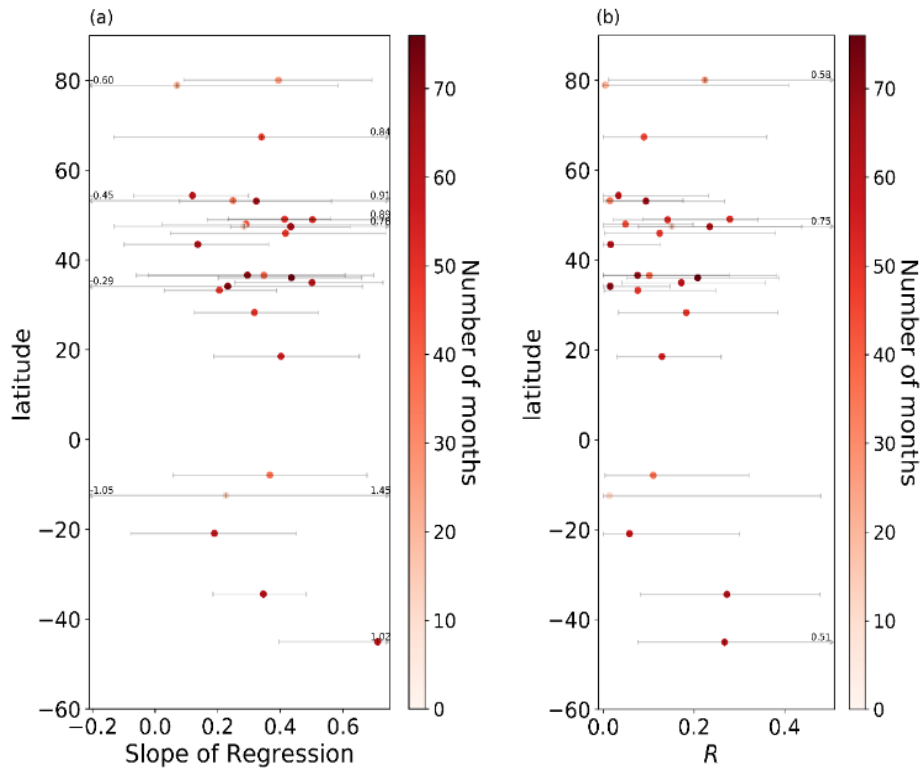440 variance between the two types of observations.

445

450

455

460

465

470 **Figure 11. Latitudinal profile of regression Slope (panel a) and correlation coefficient (R, panel b) of OCO-2 versus TCCON XCO_2 IAV. The Slope and R values are based on using monthly XCO_2 IAV. The error bars result from a Monte Carlo bootstrapping approach . The colours represent the number of months data which used for the regression calculation, given gaps in both the OCO-2 and TCCON datasets.**

16

We derive the regression slopes and Correlation Coefficient R between OCO-2 and monthly averaged TCCON IAV

475   through bootstrapping Linear Regression fitting techniques to investigate the coherence between IAV signals from space-based and in-situ ground-based observations. We compute the linear regression 1000 times, by iteratively resampling the IAV timeseries with replacement, and calculate the 95% significant level for regression slopes based on the histogram of the sample distributions during the bootstrapping (Fig. S13). Despite having similar IAV amplitudes, the IAV timeseries from OCO-2 are only moderately correlated with those from TCCON (Fig. 11). The

480   regression slopes range from 0.1- 0.6 and R values are generally around 0.1 – 0.5, indicating that less than 25% of the IAV in OCO-2 is explained by IAV measured by TCCON. These R values are, as expected, smaller than the zonal averages shown in Fig. 11b, which average some of the site-level noise for TCCON and gridcell-level noise for OCO-2. The detailed XCO_2 IAV timeseries of each site (Fig. S10) for OCO-2 and TCCON show that the IAV timeseries in the NH are more variable, which can partly explain the hemispheric difference in amplitude, slope, and correlation
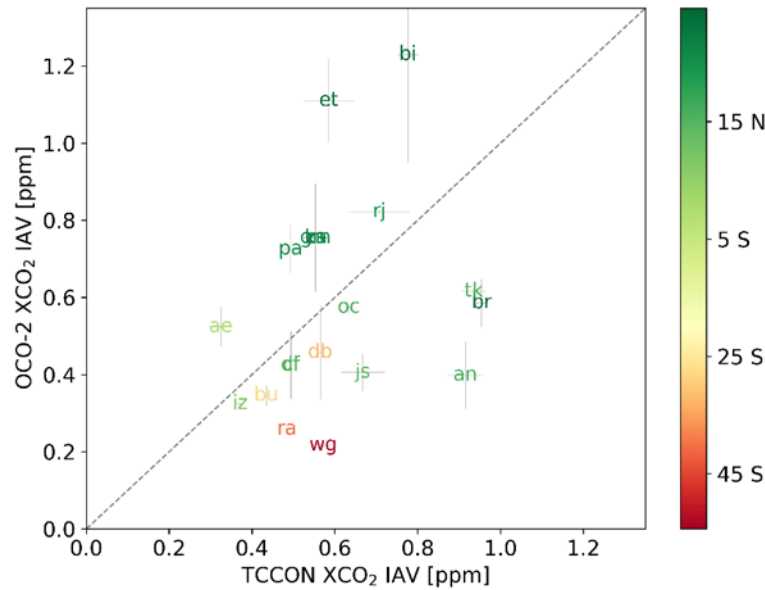
485   coefficients.

Figure 12. Comparison of OCO-2 and TCCON XCO₂ IAV amplitude at individual sites. Colours reflect site latitudes. The grey dashed line is the one-to-one identity line. The grey solid line is the error bar of the IAV amplitude.

490

4 Discussion

We use seven years of OCO-2 total column carbon dioxide observations from late 2014 to mid-2021 to illustrate the global temporal-spatial patterns of atmospheric XCO_2 interannual variations. OCO-2 and GOSAT showed reasonable agreement (Fig.4) in northern and southern hemisphere tropical zones (0-20°), although there were some notable phase

495   differences during the strong 2015 El Niño for GOSAT compared to the other timeseries in both the northern and southern extratropic regions. In contrast, OCO-2 shows good temporal agreement with the ground-based observations from MBL and TCCON. The temporal agreement of the OCO-2 and TCCON XCO_2 IAV timeseries and the MBL surface CO_2 IAV timeseries in broad zonal belts improves our confidence that we can quantify IAV timeseries from the satellite record. We note that amplitude differences remain among the timeseries, owing to two major factors: first,

500   compared to MBL surface observations, we expect XCO_2 timeseries to have smaller amplitudes of variability since it integrates over the entire atmospheric column (Olsen and Randerson 2004), and second, the fact that the OCO-2 timeseries averages around a full latitude circle rather than a few discrete sites reduces some of the IAV contained in site-level records. From the space-based and ground-based detection, we are able to characterize the global response of OCO-2 and TCCON XCO_2 or MBL surface CO_2 IAV to ENSO, and track the CO_2 IAV against the positive/negative

505   phase of ENSO, together with the transport of the signal from South to North (Fig. 4). All datasets show consistent patterns in the response to the El Niño periods, although we note that the IAV amplitude is a factor of almost two smaller in the column average mole fraction compared to the boundary layer CO_2, which reflects the fact that IAV variations emerge due to surface fluxes in the lower part of the atmosphere (Olsen & Randerson, 2004), but are efficiently transported into the free troposphere which comprises the bulk of the column. When taken together, the use

510   of surface and column data may allow better separation of transport-driven versus local flux driven variations at the interannual timescale. In the future, as partial column retrievals (e.g., Kulawik et al., 2017) mature, intercomparisons of lowermost tropospheric partial columns may provide a useful bridge between variations in surface MBL observations and total column observations.

515   Our results, however, underscore the difficulty in detecting IAV signals from remote sensing of XCO_2 -- while northern hemisphere seasonal amplitudes are typically 10 ppm scale (Basu et al., 2011), the magnitude of OCO-2 detected XCO_2 IAV is almost an order of magnitude smaller (less than 0.4 ppm over ocean and about 1ppm over continents). The magnitude of IAV is therefore comparable to other components of the XCO_2 variance budget; for instance, Torres et al. (2019) show random noise in individual OCO-2 soundings of about 0.3 ppm in the southern

520   hemisphere and of about 0.7 ppm in the northern hemisphere, and spatially coherent errors in the retrievals ranging from 0.3 to 0.8 ppm (Torres et al., 2019). Moreover, the uncertainty which originally comes from the varying climatological seasonal cycle, can also reach the level of 0.5ppm (Fig. 3d). Therefore, robust partitioning of IAV from the observed XCO_2 signal at a given location requires a comprehensive variance budget (Mitchell et al., 2023), and efforts to infer interannual variations in fluxes from OCO-2 must take gridcell-level variance into account or leverage

525   zonally averaged data, which is characterized by greater separation between IAV signal and noise.

Our analysis shows that proper spatial averaging of the monthly XCO_2 signal can mitigate the imprint of random noise and systematic effects from weather systems at sub-monthly timescales. Based on sensitivity tests, we recommend averaging low to mid-latitude of XCO_2 (equatorward of 45°) to 5°x5° bins, and 5° latitude x 10° longitude grid cell

530   poleward of 45°, ensuring that each gridcell aggregates at least 5 soundings within a month. At these levels of spatial averaging, the XCO_2 IAV amplitude was comparable to that of the co-located ground based XCO_2 IAV amplitude measured by TCCON (Fig.12). However, the moderate to low correlation between the IAV timeseries from each monitoring platform reveals the discrepancies of the two measurements in sampling, detection or retrieval, suggesting that one or both is still convolving another source of variance with the calculated IAV signal. Based on the good

535   agreement between the two timeseries in broad zonal belts, we expect that random noise in both observations may degrade the comparison.
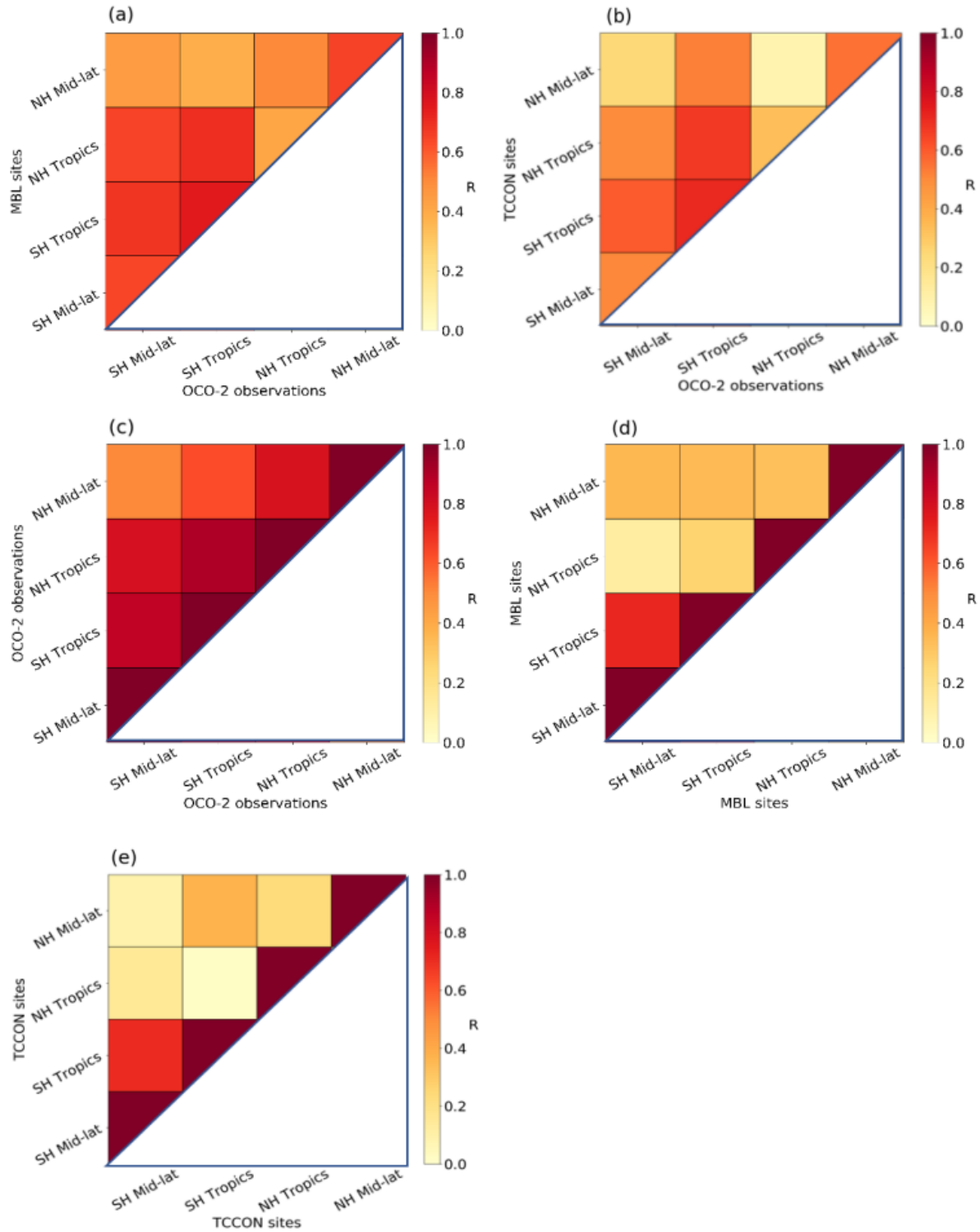
Figure 13. Correlation coefficient (R) between among mean CO_2 timeseries using three observing strategies. Panel (a) shows the correlation between zonal mean OCO-2 XCO_2 IAV and zonal mean marine boundary layer CO_2. Panel (b) shows the correlation between zonal mean XCO_2 IAV from OCO-2 and TCCON. Panels (c-e) show the correlation in zonal mean IAV timeseries across four latitude bands for a single observing strategy. Panel (c) shows OCO-2 XCO_2, Panel (d) shows MBL CO_2 and Panel (e) shows TCCON XCO_2. For Panels c-e, the diagonal elements are 1 by construction. Zonal bands include tropical (0°-20°) and NH/SH temperate zone (20°-60°).

19

545   The smaller coherence in the IAV timeseries in nearby land and ocean gridcells may be due to larger error over land or may reflect that XCO_2 observations over land contain information about heterogeneous local flux IAV. Complete analysis of the variance budget for OCO-2 observations (Mitchell et al., 2023) will elucidate the likely imprint of each process. When using IAV timeseries for flux inference, it will be crucial to account for non-flux imprints such as imprint from atmospheric transport, random errors, systematic errors, and remote geophysical coherence on the

550   timeseries (e.g., Torres et al., 2019; Mitchell et al., 2023), since spurious attribution of IAV will lead to biased fluxes.

5 Conclusions

We examined IAV in OCO-2 data to determine whether the small variations that result from interannual flux variations

555   can be detected in light of other sources of variance in the space-based dataset. Our results show that zonal averages reveal relationships with ENSO that are consistent with those from established ground-based monitoring network. Zonal averages greatly reduce random noise in XCO_2 compared to 5x5° averages. In general, OCO-2 can successfully monitor CO_2 IAV over both land and ocean, contributing important spatial coverage beyond inferences of IAV from existing ground-based networks.

560   **Data Availability**

The version 10 OCO-2 Level 2 bias-corrected XCO_2 data product is available from Goddard Earth Sciences Data and Information Services Center Archive: https://disc.gsfc.nasa.gov/datasets/OCO2_L2_Lite_FP_10r/summary. TCCON Data is publicly available from the TCCON Data Archive (https://tccondata.org/) hosted by the California Institute of Technology. MBL dry air mole fraction data is available from NOAA Global Monitoring Laboratory Earth System

565   Research Laboratories Archive: https://gml.noaa.gov/ccgg/mbl/data.php.

Author Contribution

Formal analysis: Yifan Guan. Writing – original draft preparation: Yifan Guan. Conceptualization: Gretchen Keppel-Aleks. Supervision: Gretchen Keppel-Aleks. Project administration: Gretchen Keppel-Aleks and Scott C. Doney. Writing – review & editing: Gretchen Keppel-Aleks, Scott C. Doney, Christof Petri, Dave Pollard, Debra Wunch,

570   Frank Hase, Hirofumi Ohyama, Isamu Morino, Justus Notholt, Kei Shiomi, Kim Strong, Kivi Rigel, Matthias Buschmann, Nicholas Deutscher, Paul Wennberg, Ralf Sussmann, Voltaire A. Velazco and Yao Té.

Competing Interests

The authors declare that they have no conflict of interest.

Acknowledgements

590   **References**

AMT - Improved retrievals of carbon dioxide from Orbiting Carbon Observatory-2 with the version 8 ACOS algorithm: https://amt.copernicus.org/articles/11/6539/2018/, last access: 4 April 2023.

Baker, D. F., Bell, E., Davis, K. J., Campbell, J. F., Lin, B., and Dobler, J.: A new exponentially decaying error

595   correlation model for assimilating OCO-2 column-average CO_2 data using a length scale computed from airborne lidar measurements, Geoscientific Model Development, 15, 649–668, https://doi.org/10.5194/gmd-15-649-2022, 2022.

Basu, S., Houweling, S., Peters, W., Sweeney, C., Machida, T., Maksyutov, S., Patra, P. K., Saito, R., Chevallier, F.,

600   Niwa, Y., Matsueda, H., and Sawa, Y.: The seasonal cycle amplitude of total column CO_2: Factors behind the model-observation mismatch, Journal of Geophysical Research: Atmospheres, 116, https://doi.org/10.1029/2011JD016124, 2011.

Blumenstock, T., Hase, F., Schneider, M., García, O. E., and Sepúlveda, E.: TCCON data from Izana (ES), Release

605   GGG2014.R1 (R1), https://doi.org/10.14291/TCCON.GGG2014.IZANA01.R1, 2017.

Carbon and Other Biogeochemical Cycles — IPCC: https://www.ipcc.ch/report/ar5/wg1/carbon-and-other-biogeochemical-cycles/, last access: 4 April 2023.

610   Chatterjee, A., Gierach, M. M., Sutton, A. J., Feely, R. A., Crisp, D., Eldering, A., Gunson, M. R., O'Dell, C. W., Stephens, B. B., and Schimel, D. S.: Influence of El Niño on atmospheric CO_2 over the tropical Pacific Ocean: Findings from NASA's OCO-2 mission, Science, 358, eaam5776, https://doi.org/10.1126/science.aam5776, 2017.

Cogan, A. J., Boesch, H., Parker, R. J., Feng, L., Palmer, P. I., Blavier, J.-F. L., Deutscher, N. M., Macatangay, R.,
615   Notholt, J., Roehl, C., Warneke, T., and Wunch, D.: Atmospheric carbon dioxide retrieved from the Greenhouse gases Observing SATellite (GOSAT): Comparison with ground-based TCCON observations and GEOS-Chem model calculations, Journal of Geophysical Research: Atmospheres, 117, https://doi.org/10.1029/2012JD018087, 2012.

620   Conway, T. J., Tans, P. P., Waterman, L. S., Thoning, K. W., Kitzis, D. R., Masarie, K. A., and Zhang, N.: Evidence for interannual variability of the carbon cycle from the National Oceanic and Atmospheric Administration/Climate Monitoring and Diagnostics Laboratory Global Air Sampling Network, Journal of Geophysical Research: Atmospheres, 99, 22831–22855, https://doi.org/10.1029/94JD01951, 1994.

625   Crisp, D., Fisher, B. M., O'Dell, C., Frankenberg, C., Basilio, R., Bösch, H., Brown, L. R., Castano, R., Connor, B., Deutscher, N. M., Eldering, A., Griffith, D., Gunson, M., Kuze, A., Mandrake, L., McDuffie, J., Messerschmidt, J., Miller, C. E., Morino, I., Natraj, V., Notholt, J., O'Brien, D. M., Oyafuso, F., Polonsky, I., Robinson, J., Salawitch, R., Sherlock, V., Smyth, M., Suto, H., Taylor, T. E., Thompson, D. R., Wennberg, P. O., Wunch, D., and Yung, Y. L.: The ACOS CO_2 retrieval algorithm – Part II: Global XCO_2 data characterization, Atmospheric
630   Measurement Techniques, 5, 687–707, https://doi.org/10.5194/amt-5-687-2012, 2012.

Crisp, D., Pollock, H. R., Rosenberg, R., Chapsky, L., Lee, R. A. M., Oyafuso, F. A., Frankenberg, C., O'Dell, C. W., Bruegge, C. J., Doran, G. B., Eldering, A., Fisher, B. M., Fu, D., Gunson, M. R., Mandrake, L., Osterman, G. B., Schwandner, F. M., Sun, K., Taylor, T. E., Wennberg, P. O., and Wunch, D.: The on-orbit performance of the
635   Orbiting Carbon Observatory-2 (OCO-2) instrument and its radiometrically calibrated products, Atmospheric Measurement Techniques, 10, 59–81, https://doi.org/10.5194/amt-10-59-2017, 2017.

Crowther, T. W., Glick, H. B., Covey, K. R., Bettigole, C., Maynard, D. S., Thomas, S. M., Smith, J. R., Hintler, G., Duguid, M. C., Amatulli, G., Tuanmu, M.-N., Jetz, W., Salas, C., Stam, C., Piotto, D., Tavani, R., Green, S., Bruce,
640   G., Williams, S. J., Wiser, S. K., Huber, M. O., Hengeveld, G. M., Nabuurs, G.-J., Tikhonova, E., Borchardt, P., Li, C.-F., Powrie, L. W., Fischer, M., Hemp, A., Homeier, J., Cho, P., Vibrans, A. C., Umunay, P. M., Piao, S. L., Rowe, C. W., Ashton, M. S., Crane, P. R., and Bradford, M. A.: Mapping tree density at a global scale, Nature, 525, 201–205, https://doi.org/10.1038/nature14967, 2015.

645   De Mazière, M., Sha, M. K., Desmet, F., Hermans, C., Scolas, F., Kumps, N., Metzger, J.-M., Duflot, V., and Cammas, J.-P.: TCCON data from Réunion Island (RE), Release GGG2014.R0 (GGG2014.R0), https://doi.org/10.14291/TCCON.GGG2014.REUNION01.R0/1149288, 2014.

Deutscher, N. M., Notholt, J., Messerschmidt, J., Weinzierl, C., Warneke, T., Petri, C., and Grupe, P.: TCCON data
650   from Bialystok (PL), Release GGG2014.R2 (R2), https://doi.org/10.14291/TCCON.GGG2014.BIALYSTOK01.R2, 2019.

Dlugokencky, E. J., Crotwell, A. M., Mund, J. W., Crotwell, M. J., and Thoning, K. W.: Atmospheric Nitrous Oxide Dry Air Mole Fractions from the NOAA GML Carbon Cycle Cooperative Global Air Sampling Network, 1997–
655   2020, Version: 2021- 07-30, NOAA Global Monitoring Laboratory Data Repository [data set], https://doi.org/10.14291/TCCON.GGG2014.BIALYSTOK01.R2, 2021.

Doney, S. C., Lima, I., Feely, R. A., Glover, D. M., Lindsay, K., Mahowald, N., Moore, J. K., and Wanninkhof, R.: Mechanisms governing interannual variability in upper-ocean inorganic carbon system and air–sea CO_2 fluxes:
660   Physical climate and atmospheric dust, Deep Sea Research Part II: Topical Studies in Oceanography, 56, 640–655, https://doi.org/10.1016/j.dsr2.2008.12.006, 2009.

Feely, R. A., Boutin, J., Cosca, C. E., Dandonneau, Y., Etcheto, J., Inoue, H. Y., Ishii, M., Quéré, C. L., Mackey, D. J., McPhaden, M., Metzl, N., Poisson, A., and Wanninkhof, R.: Seasonal and interannual variability of CO_2 in the
665   equatorial Pacific, Deep Sea Research Part II: Topical Studies in Oceanography, 49, 2443–2469, https://doi.org/10.1016/S0967-0645(02)00044-9, 2002.

Feist, D. G., Arnold, S. G., John, N., and Geibel, M. C.: TCCON data from Ascension Island (SH), Release GGG2014.R0 (GGG2014.R0), https://doi.org/10.14291/TCCON.GGG2014.ASCENSION01.R0/1149285, 2014.
670

Francey, R. J., Tans, P. P., Allison, C. E., Enting, I. G., White, J. W. C., and Trolier, M.: Changes in oceanic and terrestrial carbon uptake since 1982, Nature, 373, 326–330, https://doi.org/10.1038/373326a0, 1995.

Friedlingstein, P., Jones, M. W., O'Sullivan, M., Andrew, R. M., Hauck, J., Peters, G. P., Peters, W., Pongratz, J.,
675   Sitch, S., Le Quéré, C., Bakker, D. C. E., Canadell, J. G., Ciais, P., Jackson, R. B., Anthoni, P., Barbero, L., Bastos, A., Bastrikov, V., Becker, M., Bopp, L., Buitenhuis, E., Chandra, N., Chevallier, F., Chini, L. P., Currie, K. I., Feely, R. A., Gehlen, M., Gilfillan, D., Gkritzalis, T., Goll, D. S., Gruber, N., Gutekunst, S., Harris, I., Haverd, V., Houghton, R. A., Hurtt, G., Ilyina, T., Jain, A. K., Joetzjer, E., Kaplan, J. O., Kato, E., Klein Goldewijk, K., Korsbakken, J. I., Landschützer, P., Lauvset, S. K., Lefèvre, N., Lenton, A., Lienert, S., Lombardozzi, D., Marland,
680   G., McGuire, P. C., Melton, J. R., Metzl, N., Munro, D. R., Nabel, J. E. M. S., Nakaoka, S.-I., Neill, C., Omar, A. M., Ono, T., Peregon, A., Pierrot, D., Poulter, B., Rehder, G., Resplandy, L., Robertson, E., Rödenbeck, C.,

Séférian, R., Schwinger, J., Smith, N., Tans, P. P., Tian, H., Tilbrook, B., Tubiello, F. N., van der Werf, G. R., Wiltshire, A. J., and Zaehle, S.: Global Carbon Budget 2019, Earth System Science Data, 11, 1783–1838, https://doi.org/10.5194/essd-11-1783-2019, 2019.

685

Goo, T.-Y., Oh, Y.-S., and Velazco, V. A.: TCCON data from Anmeyondo (KR), Release GGG2014.R0 (GGG2014.R0), https://doi.org/10.14291/TCCON.GGG2014.ANMEYONDO01.R0/1149284, 2014.

Griffith, D. W. T., Deutscher, N. M., Velazco, V. A., Wennberg, P. O., Yavin, Y., Keppel-Aleks, G., Washenfelder, R. A., Toon, G. C., Blavier, J.-F., Paton-Walsh, C., Jones, N. B., Kettlewell, G. C., Connor, B. J., Macatangay, R. C., Roehl, C., Ryczek, M., Glowacki, J., Culgan, T., and Bryant, G. W.: TCCON data from Darwin (AU), Release GGG2014.R0 (GGG2014.R0), https://doi.org/10.14291/TCCON.GGG2014.DARWIN01.R0/1149290, 2014.

690

Griffith, D. W. T., Velazco, V. A., Deutscher, N. M., Paton-Walsh, C., Jones, N. B., Wilson, S. R., Macatangay, R. C., Kettlewell, G. C., Buchholz, R. R., and Riggenbach, M. O.: TCCON data from Wollongong (AU), Release GGG2014.R0 (GGG2014.R0), https://doi.org/10.14291/TCCON.GGG2014.WOLLONGONG01.R0/1149291, 2014.

695

Gruber, N., Keeling, C. D., and Bates, N. R.: Interannual variability in the North Atlantic Ocean carbon sink, Science, 298, 2374–2378, https://doi.org/10.1126/science.1077077, 2002.

700

Hase, F., Blumenstock, T., Dohe, S., Groß, J., and Kiel, M. ä.: TCCON data from Karlsruhe (DE), Release GGG2014.R1 (GGG2014.R1), https://doi.org/10.14291/TCCON.GGG2014.KARLSRUHE01.R1/1182416, 2015.

Iraci, L. T., Podolske, J. R., Hillyard, P. W., Roehl, C., Wennberg, P. O., Blavier, J.-F., Landeros, J., Allen, N., Wunch, D., Zavaleta, J., Quigley, E., Osterman, G. B., Albertson, R., Dunwoody, K., and Boyden, H.: TCCON data from Edwards (US), Release GGG2014.R1 (GGG2014.R1), https://doi.org/10.14291/TCCON.GGG2014.EDWARDS01.R1/1255068, 2016.

705

Karion, A., Sweeney, C., Tans, P., and Newberger, T.: AirCore: An Innovative Atmospheric Sampling System, Journal of Atmospheric and Oceanic Technology, 27, 1839–1853, https://doi.org/10.1175/2010JTECHA1448.1, 2010.

710

Kawakami, S., Ohyama, H., Arai, K., Okumura, H., Taura, C., Fukamachi, T., and Sakashita, M.: TCCON data from Saga (JP), Release GGG2014.R0 (GGG2014.R0), https://doi.org/10.14291/TCCON.GGG2014.SAGA01.R0/1149283, 2014.

715

Keppel-Aleks, G., Wennberg, P. O., Washenfelder, R. A., Wunch, D., Schneider, T., Toon, G. C., Andres, R. J., Blavier, J.-F., Connor, B., Davis, K. J., Desai, A. R., Messerschmidt, J., Notholt, J., Roehl, C. M., Sherlock, V.,

Stephens, B. B., Vay, S. A., and Wofsy, S. C.: The imprint of surface fluxes and transport on variations in total column carbon dioxide, Biogeosciences, 9, 875–891, https://doi.org/10.5194/bg-9-875-2012, 2012.

Keppel-Aleks, G., Wolf, A. S., Mu, M., Doney, S. C., Morton, D. C., Kasibhatla, P. S., Miller, J. B., Dlugokencky, E. J., and Randerson, J. T.: Separating the influence of temperature, drought, and fire on interannual variability in atmospheric CO_2, Global Biogeochem Cycles, 28, 1295–1310, https://doi.org/10.1002/2014GB004890, 2014.

Kivi, R., Heikkinen, P., and Kyrö, E.: TCCON data from Sodankylä (FI), Release GGG2014.R0 (GGG2014.R0), https://doi.org/10.14291/TCCON.GGG2014.SODANKYLA01.R0/1149280, 2014.

Kivi, R. and Heikkinen, P.: Fourier transform spectrometer measurements of column CO_2 at Sodankylä, Finland, Geoscientific Instrumentation, Methods and Data Systems, 5, 271–279, https://doi.org/10.5194/gi-5-271-2016, 2016.

Kulawik, S., Wunch, D., O'Dell, C., Frankenberg, C., Reuter, M., Oda, T., Chevallier, F., Sherlock, V., Buchwitz, M., Osterman, G., Miller, C. E., Wennberg, P. O., Griffith, D., Morino, I., Dubey, M. K., Deutscher, N. M., Notholt, J., Hase, F., Warneke, T., Sussmann, R., Robinson, J., Strong, K., Schneider, M., De Mazière, M., Shiomi, K., Feist, D. G., Iraci, L. T., and Wolf, J.: Consistent evaluation of ACOS-GOSAT, BESD-SCIAMACHY, CarbonTracker, and MACC through comparisons to TCCON, Atmospheric Measurement Techniques, 9, 683–709, https://doi.org/10.5194/amt-9-683-2016, 2016.

Le Quéré, C., Raupach, M. R., Canadell, J. G., Marland, G., Bopp, L., Ciais, P., Conway, T. J., Doney, S. C., Feely, R. A., Foster, P., Friedlingstein, P., Gurney, K., Houghton, R. A., House, J. I., Huntingford, C., Levy, P. E., Lomas, M. R., Majkut, J., Metzl, N., Ometto, J. P., Peters, G. P., Prentice, I. C., Randerson, J. T., Running, S. W., Sarmiento, J. L., Schuster, U., Sitch, S., Takahashi, T., Viovy, N., van der Werf, G. R., and Woodward, F. I.: Trends in the sources and sinks of carbon dioxide, Nature Geosci, 2, 831–836, https://doi.org/10.1038/ngeo689, 2009.

Marcolla, B., Rödenbeck, C., and Cescatti, A.: Patterns and controls of inter-annual variability in the terrestrial carbon budget, Biogeosciences, 14, 3815–3829, https://doi.org/10.5194/bg-14-3815-2017, 2017.

Masarie, K. A. and Tans, P. P.: Extension and integration of atmospheric carbon dioxide data into a globally consistent measurement record, Journal of Geophysical Research: Atmospheres, 100, 11593–11610, https://doi.org/10.1029/95JD00859, 1995.

Masson-Delmotte, V., Zhai, P., Pirani, A., Connors, S. L., Péan, C., Berger, S., Caud, N., Chen, Y., Goldfarb, L., Gomis, M. I., Huang, M., Leitzell, K., Lonnoy, E., Matthews, J. B. R., Maycock, T. K., Waterfield, T., Yelekçi, Ö., Yu, R., and Zhou, B. (Eds.): Climate Change 2021: The Physical Science Basis. Contribution of Working Group I to

the Sixth Assessment Report of the Intergovernmental Panel on Climate Change, Cambridge University Press, Cambridge, United Kingdom and New York, NY, USA, https://doi.org/10.1017/9781009157896, 2021.

McKinley, G. A., Rödenbeck, C., Gloor, M., Houweling, S., and Heimann, M.: Pacific dominance to global air-sea

760   CO_2 flux variability: A novel atmospheric inversion agrees with ocean models, Geophysical Research Letters, 31, https://doi.org/10.1029/2004GL021069, 2004.

Mitchell, K. A., Doney, S. C., and Keppel-Aleks, G.: Characterizing Average Seasonal, Synoptic, and Finer Variability in Orbiting Carbon Observatory-2 XCO_2 Across North America and Adjacent Ocean Basins, Journal of

765   Geophysical Research: Atmospheres, 128, e2022JD036696, https://doi.org/10.1029/2022JD036696, 2023.

Morino, I., Matsuzaki, T., and Horikawa, M.: TCCON data from Tsukuba (JP), 125HR, Release GGG2014.R1 (GGG2014.R1), https://doi.org/10.14291/TCCON.GGG2014.TSUKUBA02.R1/1241486, 2016.

770   Morino, I., Yokozeki, N., Matsuzaki, T., and Horikawa, M.: TCCON data from Rikubetsu (JP), Release GGG2014.R1 (GGG2014.R1), https://doi.org/10.14291/TCCON.GGG2014.RIKUBETSU01.R1/1242265, 2016.

Morino, Isamu, Velazco, Voltaire A., Hori, Akihiro, Uchino, Osamu, and Griffith, David W.T.: TCCON data from Burgos, Ilocos Norte (PH), Release GGG2020.R0 (R0),

775   https://doi.org/10.14291/TCCON.GGG2020.BURGOS01.R0, 2023.

Mudelsee, M.: Climate Time Series Analysis, Springer Netherlands, Dordrecht, https://doi.org/10.1007/978-90-481-9482-7, 2010.

780   Nassar, R., Jones, D. B. A., Kulawik, S. S., Worden, J. R., Bowman, K. W., Andres, R. J., Suntharalingam, P., Chen, J. M., Brenninkmeijer, C. a. M., Schuck, T. J., Conway, T. J., and Worthy, D. E.: Inverse modeling of CO_2 sources and sinks using satellite observations of CO_2 from TES and surface flask measurements, Atmospheric Chemistry and Physics, 11, 6029–6047, https://doi.org/10.5194/acp-11-6029-2011, 2011.

785   Notholt, J., Petri, C., Warneke, T., Deutscher, N. M., Palm, M., Buschmann, M., Weinzierl, C., Macatangay, R. C., and Grupe, P.: TCCON data from Bremen (DE), Release GGG2014.R0 (GGG2014.R0), https://doi.org/10.14291/TCCON.GGG2014.BREMEN01.R0/1149275, 2014.

Notholt, J., Warneke, T., Petri, C., Deutscher, N. M., Weinzierl, C., Palm, M., and Buschmann, M.: TCCON data

790   from Ny Ålesund, Spitsbergen (NO), Release GGG2014.R1 (R1), https://doi.org/10.14291/TCCON.GGG2014.NYALESUND01.R1, 2019.

O'Dell, C. W., Connor, B., Bösch, H., O'Brien, D., Frankenberg, C., Castano, R., Christi, M., Eldering, D., Fisher, B., Gunson, M., McDuffie, J., Miller, C. E., Natraj, V., Oyafuso, F., Polonsky, I., Smyth, M., Taylor, T., Toon, G. C., Wennberg, P. O., and Wunch, D.: The ACOS CO_2 retrieval algorithm – Part 1: Description and validation against synthetic observations, Atmospheric Measurement Techniques, 5, 99–121, https://doi.org/10.5194/amt-5-99-2012, 2012.

O'Dell, C. W., Eldering, A., Wennberg, P. O., Crisp, D., Gunson, M. R., Fisher, B., Frankenberg, C., Kiel, M., Lindqvist, H., Mandrake, L., Merrelli, A., Natraj, V., Nelson, R. R., Osterman, G. B., Payne, V. H., Taylor, T. E., Wunch, D., Drouin, B. J., Oyafuso, F., Chang, A., McDuffie, J., Smyth, M., Baker, D. F., Basu, S., Chevallier, F., Crowell, S. M. R., Feng, L., Palmer, P. I., Dubey, M., García, O. E., Griffith, D. W. T., Hase, F., Iraci, L. T., Kivi, R., Morino, I., Notholt, J., Ohyama, H., Petri, C., Roehl, C. M., Sha, M. K., Strong, K., Sussmann, R., Te, Y., Uchino, O., and Velazco, V. A.: Improved retrievals of carbon dioxide from Orbiting Carbon Observatory-2 with the version 8 ACOS algorithm, Atmospheric Measurement Techniques, 11, 6539–6576, https://doi.org/10.5194/amt-11-6539-2018, 2018.

Olsen, S. C. and Randerson, J. T.: Differences between surface and column atmospheric CO_2 and implications for carbon cycle research, Journal of Geophysical Research: Atmospheres, 109, https://doi.org/10.1029/2003JD003968, 2004.

Patra, P. K., Maksyutov, S., Ishizawa, M., Nakazawa, T., Takahashi, T., and Ukita, J.: Interannual and decadal changes in the sea-air CO_2 flux from atmospheric CO_2 inverse modeling, Global Biogeochemical Cycles, 19, https://doi.org/10.1029/2004GB002257, 2005.

Peylin, P., Bousquet, P., Le Quéré, C., Sitch, S., Friedlingstein, P., McKinley, G., Gruber, N., Rayner, P., and Ciais, P.: Multiple constraints on regional CO_2 flux variations over land and oceans, Global Biogeochemical Cycles, 19, https://doi.org/10.1029/2003GB002214, 2005.

Piao, S., Sitch, S., Ciais, P., Friedlingstein, P., Peylin, P., Wang, X., Ahlström, A., Anav, A., Canadell, J. G., Cong, N., Huntingford, C., Jung, M., Levis, S., Levy, P. E., Li, J., Lin, X., Lomas, M. R., Lu, M., Luo, Y., Ma, Y., Myneni, R. B., Poulter, B., Sun, Z., Wang, T., Viovy, N., Zaehle, S., and Zeng, N.: Evaluation of terrestrial carbon cycle models for their response to climate variability and to CO2 trends, Glob Chang Biol, 19, 2117–2132, https://doi.org/10.1111/gcb.12187, 2013.

Piao, S., Wang, X., Wang, K., Li, X., Bastos, A., Canadell, J. G., Ciais, P., Friedlingstein, P., and Sitch, S.: Interannual variation of terrestrial carbon cycle: Issues and perspectives, Glob Chang Biol, 26, 300–318, https://doi.org/10.1111/gcb.14884, 2020.

830   Randerson, J. T.: Global warming and tropical carbon, Nature, 494, 319–320, https://doi.org/10.1038/nature11949, 2013.

Schwalm, C. R., Williams, C. A., Schaefer, K., Baker, I., Collatz, G. J., and Rödenbeck, C.: Does terrestrial drought explain global CO_2 flux anomalies induced by El Niño?, Biogeosciences, 8, 2493–2506, https://doi.org/10.5194/bg-
835   8-2493-2011, 2011.

Sherlock, V., Connor, B., Robinson, J., Shiona, H., Smale, D., and Pollard, D. F.: TCCON data from Lauder (NZ), 125HR, Release GGG2014.R0 (GGG2014.R0), https://doi.org/10.14291/TCCON.GGG2014.LAUDER02.R0/1149298, 2014.
840

Strong, K., Roche, S., Franklin, J. E., Mendonca, J., Lutsch, E., Weaver, D., Fogal, P. F., Drummond, J. R., Batchelor, R., and Lindenmaier, R.: TCCON data from Eureka (CA), Release GGG2014.R2 (R2), https://doi.org/10.14291/TCCON.GGG2014.EUREKA01.R2, 2017.

845   Sussmann, R. and Rettinger, M.: TCCON data from Garmisch (DE), Release GGG2014.R1 (R1), https://doi.org/10.14291/TCCON.GGG2014.GARMISCH01.R1, 2017.

Sussmann, R. and Rettinger, M.: TCCON data from Zugspitze (DE), Release GGG2014.R1 (R1), https://doi.org/10.14291/TCCON.GGG2014.ZUGSPITZE01.R1, 2018.
850

Sussmann, R. and Rettinger, M.: Can We Measure a COVID-19-Related Slowdown in Atmospheric CO2 Growth? Sensitivity of Total Carbon Column Observations, Remote Sensing, 12, 2387, https://doi.org/10.3390/rs12152387, 2020.

855   Té, Y., Jeseck, P., and Janssen, C.: TCCON data from Paris (FR), Release GGG2014.R0 (GGG2014.R0), https://doi.org/10.14291/TCCON.GGG2014.PARIS01.R0/1149279, 2014.

Thoning, K. W., Tans, P. P., and Komhyr, W. D.: Atmospheric carbon dioxide at Mauna Loa Observatory: 2. Analysis of the NOAA GMCC data, 1974–1985, Journal of Geophysical Research: Atmospheres, 94, 8549–8565,
860   https://doi.org/10.1029/JD094iD06p08549, 1989.

Timmermann, A., An, S. I., Kug, J. S., Jin, F. F., Cai, W., Capotondi, A., Cobb, K. M., Lengaigne, M., McPhaden, M. J., Stuecker, M. F., Stein, K., Wittenberg, A. T., Yun, K. S., Bayr, T., Chen, H. C., Chikamoto, Y., Dewitte, B., Dommenget, D., Grothe, P., Guilyardi, E., Ham, Y. G., Hayashi, M., Ineson, S., Kang, D., Kim, S., Kim, W. M.,
865   Lee, J. Y., Li, T., Luo, J. J., McGregor, S., Planton, Y., Power, S., Rashid, H., Ren, H. L., Santoso, A., Takahashi,

28

K., Todd, A., Wang, G., Wang, G., Xie, R., Yang, W. H., Yeh, S. W., Yoon, J., Zeller, E., and Zhang, X.: El Niño–Southern Oscillation complexity, Nature, 559, 535–545, https://doi.org/10.1038/s41586-018-0252-6, 2018.

870 Wang, J., Zeng, N., Liu, Y., and Bao, Q.: To what extent can interannual CO2 variability constrain carbon cycle sensitivity to climate change in CMIP5 Earth System Models?, Geophysical Research Letters, 41, 3535–3544, https://doi.org/10.1002/2014GL060004, 2014.

Wang, X., Piao, S., Ciais, P., Friedlingstein, P., Myneni, R. B., Cox, P., Heimann, M., Miller, J., Peng, S., Wang, T., Yang, H., and Chen, A.: A two-fold increase of carbon cycle sensitivity to tropical temperature variations, Nature, 875 506, 212–215, https://doi.org/10.1038/nature12915, 2014.

Warneke, T., Messerschmidt, J., Notholt, J., Weinzierl, C., Deutscher, N. M., Petri, C., and Grupe, P.: TCCON data from Orléans (FR), Release GGG2014.R0 (GGG2014.R0), https://doi.org/10.14291/TCCON.GGG2014.ORLEANS01.R0/1149276, 2014.

880
Washenfelder, R. A., Toon, G. C., Blavier, J.-F., Yang, Z., Allen, N. T., Wennberg, P. O., Vay, S. A., Matross, D. M., and Daube, B. C.: Carbon dioxide column abundances at the Wisconsin Tall Tower site, Journal of Geophysical Research: Atmospheres, 111, https://doi.org/10.1029/2006JD007154, 2006.

885 Wennberg, P. O., Roehl, C. M., Wunch, D., Toon, G. C., Blavier, J.-F., Washenfelder, R., Keppel-Aleks, G., Allen, N. T., and Ayers, J.: TCCON data from Park Falls (US), Release GGG2014.R1 (GGG2014.R1), https://doi.org/10.14291/TCCON.GGG2014.PARKFALLS01.R1, 2017.

Wennberg, P. O., Wunch, D., Roehl, C. M., Blavier, J.-F., Toon, G. C., and Allen, N. T.: TCCON data from Caltech 890 (US), Release GGG2014.R1 (GGG2014.R1), https://doi.org/10.14291/TCCON.GGG2014.PASADENA01.R1/1182415, 2015.

Wennberg, P. O., Wunch, D., Roehl, C. M., Blavier, J.-F., Toon, G. C., and Allen, N. T.: TCCON data from Lamont (US), Release GGG2014.R1 (GGG2014.R1), 895 https://doi.org/10.14291/TCCON.GGG2014.LAMONT01.R1/1255070, 2016.

Wu, L., aan de Brugh, J., Meijer, Y., Sierk, B., Hasekamp, O., Butz, A., and Landgraf, J.: XCO_2 observations using satellite measurements with moderate spectral resolution: investigation using GOSAT and OCO-2 measurements, Atmospheric Measurement Techniques, 13, 713–729, https://doi.org/10.5194/amt-13-713-2020, 2020.

900

Wunch, D., Mendonca, J., Colebatch, O., Allen, N. T., Blavier, J.-F., Roche, S., Hedelius, J., Neufeld, G., Springett, S., Worthy, D., Kessler, R., and Strong, K.: TCCON data from East Trout Lake, SK (CA), Release GGG2014.R1 (R1), https://doi.org/10.14291/TCCON.GGG2014.EASTTROUTLAKE01.R1, 2018.

905   Wunch, D., Toon, G. C., Wennberg, P. O., Wofsy, S. C., Stephens, B. B., Fischer, M. L., Uchino, O., Abshire, J. B., Bernath, P., Biraud, S. C., Blavier, J.-F. L., Boone, C., Bowman, K. P., Browell, E. V., Campos, T., Connor, B. J., Daube, B. C., Deutscher, N. M., Diao, M., Elkins, J. W., Gerbig, C., Gottlieb, E., Griffith, D. W. T., Hurst, D. F., Jiménez, R., Keppel-Aleks, G., Kort, E. A., Macatangay, R., Machida, T., Matsueda, H., Moore, F., Morino, I., Park, S., Robinson, J., Roehl, C. M., Sawa, Y., Sherlock, V., Sweeney, C., Tanaka, T., and Zondlo, M. A.: Calibration of
910   the Total Carbon Column Observing Network using aircraft profile data, Atmospheric Measurement Techniques, 3, 1351–1362, https://doi.org/10.5194/amt-3-1351-2010, 2010.

Wunch, D., Toon, G. C., Sherlock, V., Deutscher, N. M., Liu, C., Feist, D. G., and Wennberg, P. O.: Documentation for the 2014 TCCON Data Release, https://doi.org/10.14291/TCCON.GGG2014.DOCUMENTATION.R0/1221662,
915   2015.

Wunch, D., Toon, G. C., Blavier, J.-F. L., Washenfelder, R. A., Notholt, J., Connor, B. J., Griffith, D. W. T., Sherlock, V., and Wennberg, P. O.: The total carbon column observing network, Philos Trans A Math Phys Eng Sci, 369, 2087–2112, https://doi.org/10.1098/rsta.2010.0240, 2011.
920

Wunch, D., Wennberg, P. O., Osterman, G., Fisher, B., Naylor, B., Roehl, C. M., O'Dell, C., Mandrake, L., Viatte, C., Kiel, M., Griffith, D. W. T., Deutscher, N. M., Velazco, V. A., Notholt, J., Warneke, T., Petri, C., De Maziere, M., Sha, M. K., Sussmann, R., Rettinger, M., Pollard, D., Robinson, J., Morino, I., Uchino, O., Hase, F., Blumenstock, T., Feist, D. G., Arnold, S. G., Strong, K., Mendonca, J., Kivi, R., Heikkinen, P., Iraci, L., Podolske,
925   J., Hillyard, P. W., Kawakami, S., Dubey, M. K., Parker, H. A., Sepulveda, E., García, O. E., Te, Y., Jeseck, P., Gunson, M. R., Crisp, D., and Eldering, A.: Comparisons of the Orbiting Carbon Observatory-2 (OCO-2) X_{CO2} measurements with TCCON, Atmospheric Measurement Techniques, 10, 2209–2238, https://doi.org/10.5194/amt-10-2209-2017, 2017.

930   Zeng, N., Mariotti, A., and Wetzel, P.: Terrestrial mechanisms of interannual CO_2 variability: INTERANNUAL CO_2 VARIABILITY, Global Biogeochem. Cycles, 19, https://doi.org/10.1029/2004GB002273, 2005.